Futile wound healing drives mesenchymal-like cell phenotypes in human glioblastoma

Alejandro Mossi Albiach[1,*]†, Jokubas Janusauskas[1]†, Jesper Kjaer Jacobsen[1,2]†, Ivana Kapustová[1], Razieh Karamzadeh[1], Egle Kvedaraite[1,3], Lijuan Hu[1], Marina C. M. Franck[1], Camiel Mannens[1,4,5,6], Simone Codeluppi[1,**], Johannes B. Munting[1], Lars E. Borm[1,4,5,6], Alia Shamikh[3,7], Peter Lönnerberg[1], Kimberly A. Siletti[1,8], Oscar Persson[9,10], Sten Linnarsson[1#]

† These authors contributed equally
# Lead contact
Correspondence to: S.L. (sten.linnarsson@ki.se)

[1] Department of Medical Biochemistry and Biophysics, Karolinska Institute, 17177 Stockholm, Sweden
[2] Department of Neurology, Karolinska University Hospital, 17164 Stockholm, Sweden
[3] Department of Clinical Pathology and Cancer Diagnostics, Karolinska University Hospital, 17164 Stockholm, Sweden
[4] Center for Brain & Disease Research, VIB, 3000 Leuven, Belgium
[5] Center for AI & Computational Biology, VIB, 3000 Leuven, Belgium
[6] Department of Human Genetics, KU Leuven, 3000 Leuven, Belgium
[7] Department of Oncology-Pathology, Karolinska Institute, 17177 Stockholm, Sweden
[8] Department of Translational Neuroscience, University Medical Center Utrecht, 3584 CG Utrecht, The Netherlands
[9] Department of Clinical Neuroscience, Karolinska Institute, 17177 Stockholm, Sweden
[10] Department of Neurosurgery, Karolinska University Hospital, 17164 Stockholm, Sweden
*Current affiliation: San Diego Institute of Science, Altos Labs, San Diego, CA, USA.
**Current affiliation: Moleculent, 17165 Stockholm, Sweden

ABSTRACT

Glioblastoma is the deadliest brain cancer, characterized by large cellular diversity whose complexity and organizing principles are only starting to be uncovered. Both neurodevelopment-like and mesenchymal-like cell states have been described in glioblastoma[1–8], with the latter being strongly implicated in malignancy and disease progression[8–11]. However, the nature of these mesenchymal-like cell states remains unresolved. Here, we performed deep single-cell RNA sequencing of rare glioblastoma cases where tissue could be sampled from tumor core to macroscopically normal cortex. We discovered that previously defined mesenchymal-like tumor cell states instead represented a wound response that was shared across both malignant and non-malignant cell types and was spatially confined to the tumor bulk. Using glioblastoma organoids, we showed that the wound response transcriptional state could be reversibly induced *in vitro* by hypoxia and human plasma. We used multiplex single-molecule spatial transcriptomics[12] on a large patient cohort to show that the activation of wound response states was associated with hypoxia, and organized by distance to perivascular niches. Our findings help reconceptualize the cellular landscape of glioblastoma, wherein a reactive wound-response tissue state shared by all cells in the tumor bulk is superimposed on a fundamentally neurodevelopmental and glial tumor.

MAIN

Glioblastoma (GBM) is the most common malignant brain cancer in adults with a median survival of less than a year[13]. While heterogeneous, these tumors nevertheless show phenotypical convergence to common cell states, oftentimes resembling neurodevelopmental lineages and commonly described as astrocyte (AC)-like, oligodendrocyte precursor cell (OPC)-like, neural progenitor cell (NPC)-like, and mesenchymal (MES)-like[1–8]. MES-like tumor cells have been associated with poor prognosis and relapse[8,9], invasiveness[10] and resistance to therapy[10,11]. This clinical importance has sparked investigations into the nature of the MES-like state[14–16] as well as efforts to identify factors that endogenously induce the MES-

like phenotype or that pharmacologically block it, as a potential therapy[17–19]. Tumor-associated macrophages (TAMs) have also been shown to induce MES-like cell states[20], and attempts have been made to target TAMs therapeutically in order to hinder tumor growth[21–23]. However, in mouse models, depletion of TAMs does not slow tumor growth[24] and can even promote it[25]. Taken together, pinpointing the causal roles of MES-like tumor cells remains a challenging yet central issue in GBM research.

Moreover, GBM surgery follows the principle of maximal safe resection of the MRI contrast-enhancing component, inevitably leaving behind infiltrating tumor cells in the tumor periphery that ultimately cause relapse[26]. This also defines tissue availability, meaning that nearly all previous studies have focused on the contrast-enhancing tumor part (although notable exceptions exist[27,28]) and that our understanding of tumor cell states beyond the tumor bulk is likewise limited. Therefore, to elucidate the role and function of MES-like cell states in GBM, here we took advantage of rare temporal lobectomies, where tissue sampling beyond the tumor margin and into macroscopically unaffected cortex was possible. We performed deep single-cell RNA sequencing on a couple of multi-region GBM cases – sampling more than 100,000 cells each – and spatial transcriptomics using 888-plex Enhanced ELectric single-molecule Fluorescence *in situ* Hybridization (EEL-FISH)[12] on multi-region samples as well as standard resection samples for a total of 41 tissue samples from 27 gliomas: 25 GBMs and two cases of oligodendroglioma (IDH-mutated, 1p19q co-deleted).

Mesenchymal-like gene expression is regulated spatially across cell types

To understand the large-scale spatial distribution of MES-like tumor cells, we first examined a rare case of GBM (sample SL040), where location of the tumor required surgical resection far outside of the MRI contrast-enhancing zone. Samples were annotated based on 5-aminolevulinic acid (5-ALA, Gliolan) fluorescence (Methods**, Fig. 1a, Extended Data Fig. 1a**); wherein high fluorescence largely corresponds to the contrast-enhancing zone[29]. We collected tissue from five nested zones: the necrotic core (central tumor mass, low or no fluorescence), high-fluorescence zone (representing the contrast-enhancing zone), low-fluorescence zone (immediately surrounding the high-fluorescence zone), tumor periphery and the surrounding cortex (**Fig. 1a**, **Extended Data Fig. 1b**). Multiple samples were taken in different directions (anterior, posterior, superior, inferior), for a total of 12 sampling locations (Methods**, Extended Data Fig. 1b**).

We used droplet single-cell RNA sequencing (scRNA-seq) to collect 135,482 single-cell transcriptomes (after quality control (QC), Methods). We classified cells as malignant or non-malignant by inferred genomic copy number variations (CNVs) using infercnvpy[30] (Methods, **Extended Data Fig. 1c**). We used established marker genes to identify astrocytes, B/plasma cells, endothelial cells, fibroblasts, macrophages, microglia, monocytes, oligodendrocytes, OPCs, pericytes, T/NK cells, tumor-associated macrophages (monocyte-derived, moTAMs), tumor-associated microglia (mgTAMs), tumor cells, vascular smooth muscle cells (Methods, **Fig. la, Extended Data Fig. 1d)**. We validated our myeloid cell annotation with a label transfer from an external dataset[31]. Tumor cells were highly frequent in the necrotic core and high-fluorescence zone (43 – 65% tumor cells). These two zones will henceforth be collectively referred to as the tumor bulk. Tumor cell frequency remained high in the low-fluorescence zone (25%, 65%), dropping sharply in the periphery, albeit with high variability across anatomical directions (0.2 – 10%; **Fig. la, Extended Data Fig. 1d**). The high frequency of tumor cells in the low-fluorescence zone, just outside the high-fluorescence zone (contrast-enhancing zone) is in line with previous findings[26]. Myeloid cells were also organized with high regional

specificity: moTAMs in the necrotic core, a mix of moTAMs and mgTAMs in the high-fluorescence zone, microglia in the low-fluorescence zone, periphery and cortex (**Fig. la, Extended Data Fig. 1d**). The relative abundance of both healthy brain cell types (microglia and astrocytes) and tumor cells in the low-fluorescence zone likely reflects that tumor cell infiltration precedes shifts in other cell populations here. This, together with the corresponding high cell cycle scores (**Fig. 1a)**, implicates the low-fluorescence zone as a niche resembling 'early-stage' tumor growth, before bulk formation, substantiating the rationale behind ongoing trials of supramarginal resection of GBM[32,33].

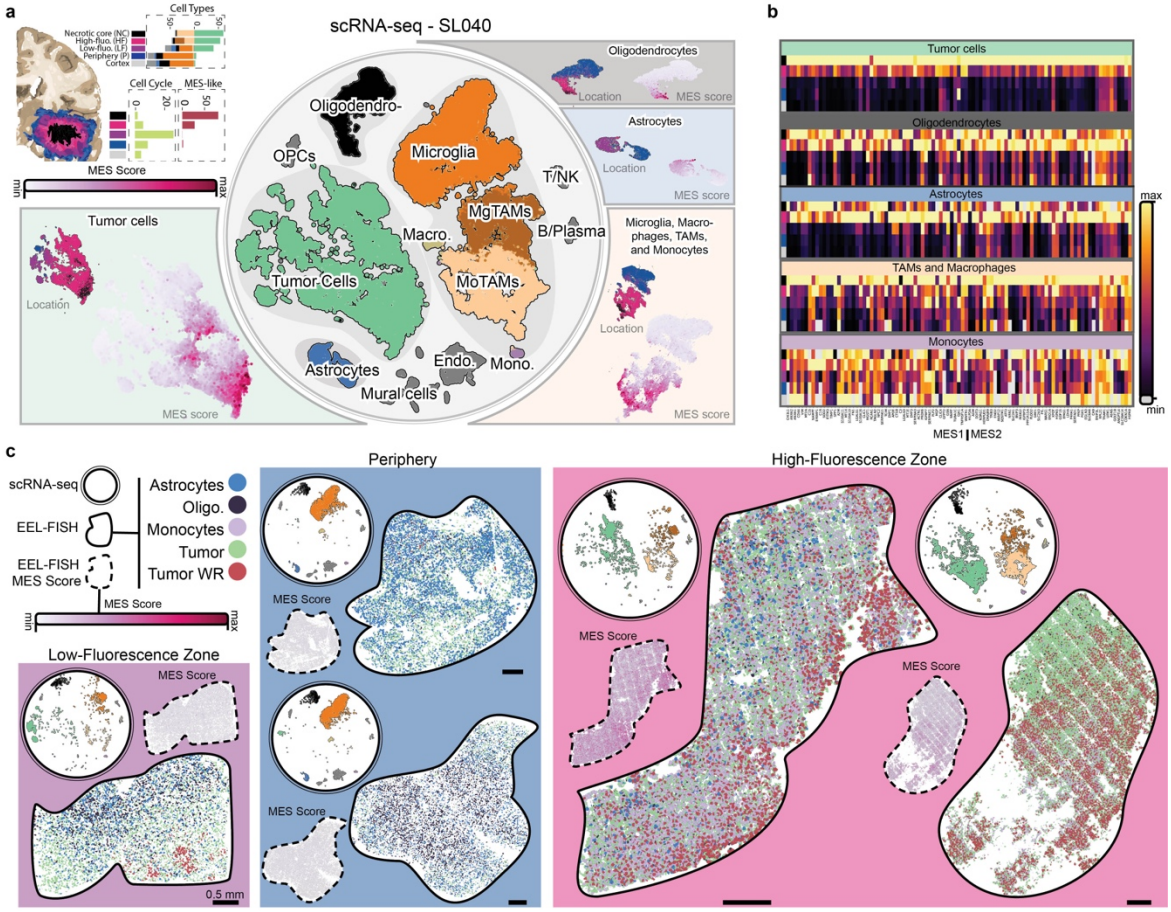

Figure 1. scRNA-seq and EEL-FISH characterization of a multi-region GBM sample. a, Top-left: schematic illustration of the organization of the fluorescence zones in GBM as part of a coronal brain section: necrotic core, high-fluorescence zone, low-fluorescence zone, periphery and cortex; cell cycle score and fraction of MES-tumor cells across different tumor zones. Center: t-distributed stochastic neighbor embedding (t-SNE) representation of scRNA-seq data from multi-region sample SL040. Surrounding the center: plots of regional distribution and MES score for tumor cells, astrocytes, oligodendrocytes, monocytes, microglia, macrophages, TAMs and other major cell types. **b,** MES-like gene expression across cell types and fluorescence zones. The colormap shows linear gene expression truncated at the 99.5% percentile, from the minimum to the maximum value per gene, with zeros shown in gray. **c,** Tumor cells (WR and non-WR), non-malignant astrocytes, oligodendrocytes and monocytes in multi-region sample SL040 as detected by EEL-FISH (full outline), corresponding MES-scores (dashed outline) and t-SNE representations of matched scRNA-seq data (circles). Low-fluorescence zone: sample SL040C; periphery: samples SL040F (top) and SL040D (bottom); high-fluorescence zone: samples SL040B (top) and SL040E (bottom).

We found a strong regional specificity of the MES-like gene signature[5] along the core-to-periphery axis, with highest expression levels in the tumor core (**Fig. 1a**, **Extended Data Fig.**

119 **1d)** in concordance with previous reports[34]. Outside the bulk, even in the low-fluorescence
120 zone where tumor cell frequency remained high, MES-like cells were nearly absent (**Extended**
121 **Data Fig. 1d**). Moreover, the expression of MES-like gene signature was not confined to
122 malignant cells: astrocytes, oligodendrocytes and TAMs, among others, all exhibited varying
123 expression levels of MES-like signature, universally increasing from periphery to core
124 (**Fig. 1a,b**, **Extended Data Fig. 1e,f**). Nearly every gene of the MES-like signature was
125 expressed and regulated in the same pattern in all cell types, and only a small set of genes (e.g.,
126 *GJA1* in astrocytes or *CLIC4* in oligodendrocytes) showed cell type-specific regulation
127 (**Fig. 1b**). The most conspicuous exception was monocytes, where MES genes were generally
128 not highly expressed or did not show regulation from core to periphery (**Fig. 1a**,**b, Extended**
129 **Data Fig. 1f**). We conclude that MES-like gene expression is a shared feature of many cell
130 types and is not an intrinsic tumor cell state, but a spatially determined tissue state confined to
131 the tumor bulk. We confirmed these findings on a second GBM case (123,236 cells after QC;
132 **Extended Data Fig. 2a,c,d)** and on an external dataset[27](3589 cells after QC; **Extended Data**
133 **Fig. 2e,f**).

134 **Wound response as a generic feature of glioblastoma**

135 The discovery that MES-like cell states are strongly regionalized and not tumor-specific
136 prompted us to reconsider the interpretation of this gene expression module. The MES-like cell
137 state in GBM was originally described based on bulk microarray gene expression profiles[1,8].
138 However, a gene ontology reanalysis of that data revealed no terms related to mesenchymal
139 cells or processes, but rather to neural development and to wound healing, blood coagulation
140 and apoptosis (**Supplementary Table 1**). Subsequently, Neftel *et al.* used single-cell
141 transcriptomics to define two MES-like GBM cell states (MES1 and MES2)[5]. Gene ontology
142 analyses of these gene sets returned no terms related to mesenchymal states or processes;
143 instead, common significant terms were related to complement activation, plasma membrane
144 repair, wound healing and coagulation (**Supplementary Table 1**). Namely, many MES1 genes
145 are functionally involved in complement activation, plasma membrane repair, plasminogen
146 activation and coagulation, all of which are related to hemostasis, i.e. the extravascular clotting
147 of extravasated blood or plasma. For MES2, we found terms related mainly to hypoxia and
148 none related to mesenchymal states or processes. A considerable fraction of MES2 genes are
149 known direct targets of HIF1α, the master regulator of hypoxic responses (16 of 50 genes).
150 Furthermore, all four Neftel *et al.* tumor cell states maintained the expression of glial master
151 transcription factor *SOX2*, whereas functional mesenchymal marker genes (collagens,
152 epithelial-to-mesenchymal, i.e. EMT, transcription factors) were either not expressed or
153 expressed at low levels and not specific to MES-like cells (**Extended Data Fig. 3a**). Thus,
154 these previously described MES-like gene sets seem neither mesenchymal nor specific to tumor
155 cells. Instead, a detailed re-examination points to hypoxia, inflammation, injury, wound
156 healing, blood clotting, and similar processes (**Supplementary Table 1**); that is, to a reactive
157 wound-healing tissue state rather than a mesenchymal differentiation process. We therefore
158 propose that the previously named mesenchymal-like cell states in GBM more likely represent
159 fundamentally glial ($SOX2^{+}$) tumor cells but with strong activation of hypoxia and wound
160 healing responses analogous to those found in normal astrocytes during brain wound repair[35].

161 To substantiate the hypothesis of MES gene involvement in wound healing responses, we
162 examined their temporal response in three tumor-free injury settings. First, in a well-powered
163 time course study of mouse skin wound healing[36] (**Extended Data Fig. 3b**), all but one MES-

164 core[37] gene was robustly and significantly (FDR < 0.05, fold-change > 1.2) induced in the acute
165 phase of wound response; *S100a16* was instead repressed in the late phase. Second, 23 of 28
166 MES-core genes were significantly (FDR < 0.05) induced in astrocytes in a mouse spinal cord
167 injury model[38] (**Extended Data Fig. 3c**). Finally, in human brain tissue resected 8 – 180 hours
168 after traumatic brain injury[39], 17 MES-like[5] genes were significantly induced in astrocytes (four
169 were down-regulated; n=12 patients and 5 controls, $P < 10^{-7}$ and absolute $\log_2$ fold change >
170 0.25 as reported in the original publication; **Extended Data Fig. 3d**).

171 Curiously, we noticed that cells in the tumor bulk expressed far more mRNA in total, as
172 compared with cells from the periphery: this was significant in tumor cells, TAMs, astrocytes,
173 vascular cells, but not in oligodendrocytes (**Extended Data Fig 2b**). The mean number of reads
174 per cell in bulk and periphery were similar across samples, but samples from bulk were
175 generally less saturated despite a higher number of detected genes and unique molecular
176 identifiers (UMIs) per cell. To discover which genes contributed most to this increase in overall
177 mRNA abundance, we performed differential gene expression analysis between tumor bulk
178 and periphery (**Extended Data Fig 1f, 2d,f**). Nearly all MES-like genes were upregulated in
179 the tumor bulk across cell types, even when normalizing for total mRNA count. Furthermore,
180 of the top upregulated genes in the bulk, the majority were MES-like genes and many of the
181 remaining genes were closely related. Thus, we conclude that gene expression in the tumor
182 bulk is dominated by a strongly induced transcriptional program, across tumor cells and most
183 non-tumor cell types, that comprises mainly MES-like genes and closely related genes
184 representing a wound healing response. We will therefore henceforth refer to them as 'wound
185 response' (WR) cell states. We computed a consensus WR gene signature across cell types and
186 samples (**Supplementary Table 2**). Reproducibility per cell type between samples was
187 remarkably high with almost 40-50% overlap in the top ranking 500 genes, with the
188 mismatched genes usually appearing in the following 500 genes (top 1000 genes). In addition
189 to previously defined MES-like gene signatures, we found 19 transcription factors associated
190 with the WR state (top 500 genes), including cAMP response-element binding protein (CREB)
191 family genes *ATF5* and *CREB3*, C/EBP family *DDIT3* (the only TF in the previous MES-like
192 signature), immediate-early genes *EGR2* and *FOSL2*, and *NFIL3* which controls expression of
193 the inflammatory cytokine IL3. These factors provide a gene regulatory basis for activation of
194 the WR phenotype in diverse cell types. Based on the enriched gene sets and our gene ontology
195 analyses, it is likely that additional related processes such as inflammation, apoptosis, and
196 metabolic rewiring also characterize these cellular states.

197 **Developmental and wound response states account for tumor cell diversity**

198 To further investigate the nature of WR states, we expanded our cohort with standard samples
199 of the bulk and mainly the contrast-enhancing tumor region, which largely correspond to the
200 high-fluorescence zone and where WR states should be most abundant (totaling 25 GBMs and
201 2 oligodendrogliomas; **Supplementary Table 3**). We trained a graph attention neural network
202 (GAT) to identify common molecular patterns across all samples by gene expression and
203 spatial proximity (**Extended Data Fig. 5a**). The GAT output was clustered into molecular
204 states (m-states) that distinguished microscale regions throughout the tissue, corresponding to
205 cell transcriptional states or cell types. Cell segmentation by m-state yielded single cells
206 (m-cells). In total, 42 shared m-states in 6,463,910 segmented m-cells (after QC; Methods)
207 were identified from 11,081,393 imaged nuclei (**Extended Data Fig. 5a**). For initial
208 annotation, we used Tangram[40] to transfer cluster labels from a GBM scRNA-seq meta-
209 analysis[41]. Most m-states mapped to either vascular, immune (validated by flow cytometry;

210 **Extended Data Fig. 4a,b**) cell types or the four canonical tumor cell states (**Extended Data**
211 **Fig. 5b**). To better distinguish non-malignant astrocytes from tumor AC-like cells, we trained
212 a classifier on the matched scRNA-seq and EEL-FISH data from multi-region sample SL040.
213 After confirming that the classifier could discriminate between astrocytes and AC-like m-cells
214 in unseen sample with multi-regional representation (**Extended Data Fig. 4c**), we applied it to
215 the remainder of the dataset. Most cell types showed strong core-to-periphery dichotomy, in
216 agreement with our scRNA-seq data: oligodendrocytes and astrocytes were found primarily in
217 the periphery, while tumor cells, despite infiltrating beyond the tumor bulk, were found in WR
218 state predominantly within the high-fluorescence zone and only in small, sparse patches outside
219 of it, matching the spatial distribution of the MES signature (**Fig. 1c**). Thus, despite reports of
220 MES-like state association with recurrence[8,9], such cells were almost completely absent from
221 the peripheral tumor regions that remain after resection.

222 Since the molecular diversity captured in our dataset exceeded the conventional nomenclature,
223 we expanded our m-state classification using a recently published scRNA-seq dataset covering
224 the first trimester of human brain development[42] (**Extended Data Figure 5b**). We re-classified
225 a total of 3,860,755 tumor m-cells by similarity to developmental cell types using Tangram,
226 introducing glioblast (GBL)-like, neural intermediate progenitor cell (nIPC)-like, preOPC-like,
227 and radial glia (RG)-like cell state labels. GBL-like and preOPC-like m-states were marked by
228 the expression of *EDNRB* and *EGFR*[43,44] (**Extended Data Fig. 6a**). In addition to the high
229 *EGFR* levels, preOPC-like m-state also showed transcriptional resemblance to outer radial glia
230 (*PTPRZ1*, *ITM2C*, *FABP7*, *EDNRB*), late glioblasts[42] or the newly-described tripotential
231 intermediate progenitor cells[45], thus representing a less differentiated state than the initially
232 assigned AC-like label (**Extended Data Fig. 5b**: II, **6a**). The nIPC-like m-states were defined
233 by expression of *SOX2*, *MDM2, CNTN1* and/or *TCF7* (**Extended Data Fig. 6a**). Two m-states
234 marked by expression of *SOX2*, *NES* and *VIM* mapped to radial glia and were accordingly
235 named RG-like and RG-nIPC-like. The more ambivalent RG-nIPC-like classification stemmed
236 from co-expression of *CDK4* and *GLI1*: the former has been linked to NPC-like cells in GBM[5]
237 and the latter is normally expressed in radial glia of the neocortex[46]. These newly annotated
238 cell states generally coexisted with the canonical glia-like states and an abundance of WR cells
239 (**Extended Data Fig. 6a**). Cases where glia-like m-cells vastly outnumbered WR m-cells (<5%
240 of WR m-cells) were few but notably included the two oligodendrogliomas and mainly multi-
241 region samples from outside the bulk (**Extended Data Fig. 6b**).

242 We subclassified WR m-states primarily by *VEGFA* expression levels and secondarily by other
243 markers: *MDM2*, *PDGFRA*, *MGP, TNC* and *TIMP1* (**Extended Data Fig. 6a**). Multiple genes
244 implicated in hypoxic and wound responses[47] were characteristic of WR m-states: *VEGFA*,
245 *LGALS1*, *SERPINE1*, *IGFBP5*, *ANXA1*, *MGP*, *TIMP1*. In contrast, we did not observe
246 expression of true mesenchyme-specific genes such as type I or III collagens, suggesting that
247 WR m-states were not of true mesenchymal identity. In part, the diversity of WR m-states
248 reflected that of glia-like m-states: WR OPC expressed *PDGFRA,* a marker of OPC-like states,
249 whereas WR nIPC expressed *MDM2*, linking it to nIPC-like 3 m-state (**Extended Data Fig.**
250 **6a**). The expression of hypoxia-response genes and the absence of mesenchymal markers in
251 WR m-states supports the reactive state hypothesis; the transcriptional similarities might
252 furthermore inform on the underlying glia-like identities.

253 **Wound response state is distinct from a fibroblast-like identity**

254 To compare the newly-proposed WR and the conventional MES-like states, we examined the
255 expression of mesenchymal and fibroblast markers, EMT transcription factors and the glial
256 transcription factor *SOX2* in the original GBM cell state classification by Neftel *et al.*[5]
257 (**Extended Data Fig. 3a**). All malignant cell states maintained *SOX2* expression, unlike true

258 fibroblasts or mesenchymal stem cells surveyed as non-malignant references[48]. Mesenchymal,
259 fibroblast and EMT markers, while detectable to varying degrees, were not specific to the
260 MES-like cell state. In fact, a single sample, pediatric glioblastoma BT830, accounted for
261 nearly all fibroblast-like gene expression (collagens *COL1A1*, *COL1A2*, *COL3A1*, collagen
262 cross-linkers *DCN* and *LUM*, but not *COL2A1* which is specific to cartilage) in the dataset
263 (**Extended Data Fig. 3a**). Furthermore, these cells expressed markers of neural crest stem cells
264 (*SOX10* and *NGFR*) and developing meningeal fibroblasts (*FOXC1*). Thus, the mesenchymal
265 characteristics in the conventional definition of the MES-like state seem specific only to a small
266 subpopulation of cells.

267 We analogously identified three distinctly fibroblast (FB)-like m-states in our EEL-FISH data,
268 characterized by such fibroblast markers as *DCN* and *COL3A1* (**Extended Data Fig. 6a**). These
269 m-states were found predominantly, albeit not exclusively, in two samples of gliosarcoma, a
270 well-known subtype of glioblastoma characterized by a glial and a sarcomatous component
271 (SL016A and SL020; **Extended Data Fig. 7a**). The $DCN^{+}TIMP1^{+}COL3A1^{+}$ FB-like 3 m-state
272 (**Extended Data Fig. 6a**), the most fibroblast-differentiated in our classification, was found
273 abundantly in both gliosarcoma samples, coexisting with WR m-states (**Extended Data Fig.
274 7b**). Unlike the FB-like m-states, none of the WR states or other major gliosarcoma constituents
275 (AC-like and RG-nIPC-like m-cells) were gliosarcoma-specific. In sample SL016A, $COL1A1^{+}$
276 FB-like m-cells were positioned around endothelial ($RGCC^{+}$) m-cells, as could be expected
277 from fibroblast-like cells, and were in turn surrounded by $VEGFA^{+}$ hypoxic WR m-states
278 **(Extended Data Fig. 7b**). This vasculature-centered organization, however, was not universal:
279 the AC-like-dominated sample SL020 showed far less of this perivascular organization, with
280 FB-like m-cells being more spatially segregated. Such hubs of FB-like m-cells, marked by
281 *TIMP1* expression, were found in both gliosarcoma samples (**Extended Data Fig. 7c**). Taken
282 together, it appears that FB-like states have previously been subsumed under the conventional
283 MES-like state, which, in turn, can be split into: (1) a reactive WR state not specific to tumor
284 cells, and (2) a rare fibroblast-like tumor cell population enriched in gliosarcoma.

285 **Wound response is an inducible and reversible cell state**

286 To test our hypothesis that WR is a modular and reactive state, we performed *in vitro*
287 perturbations of glioblastoma organoids (GBOs) derived from four GBM patients. Given the
288 expression of hypoxia and hemostasis-related genes in WR-states, we selected hypoxia and
289 blood plasma as two candidate inducers. We subjected GBOs to either condition, or a
290 combination of both, for 72 hours to test the inducibility, and reverted to regular media and
291 normoxia for another 72 hours to assess the reversibility of WR state activation, performing
292 Xenium spatial transcriptomics analysis at several timepoints (Methods; **Fig. 2a**). We
293 integrated data from all four GBO lines using scVI[49] and found a range of glia-like states
294 corresponding to those observed in tumor samples, but only few non-malignant glial, immune
295 or vascular cells (**Extended Data Fig. 8a**). We also found two hypoxic response states (+HYP1
296 and +HYP2) that resembled our previously described WR m-states by expression of *ANXA1/2*,
297 *CD44*, *EPAS1, HILPDA* and *VEGFA*, among other markers. Cell states were reproducible
298 across the different GBO lines even when not correcting for batch effects (**Extended Data Fig.
299 8b**).

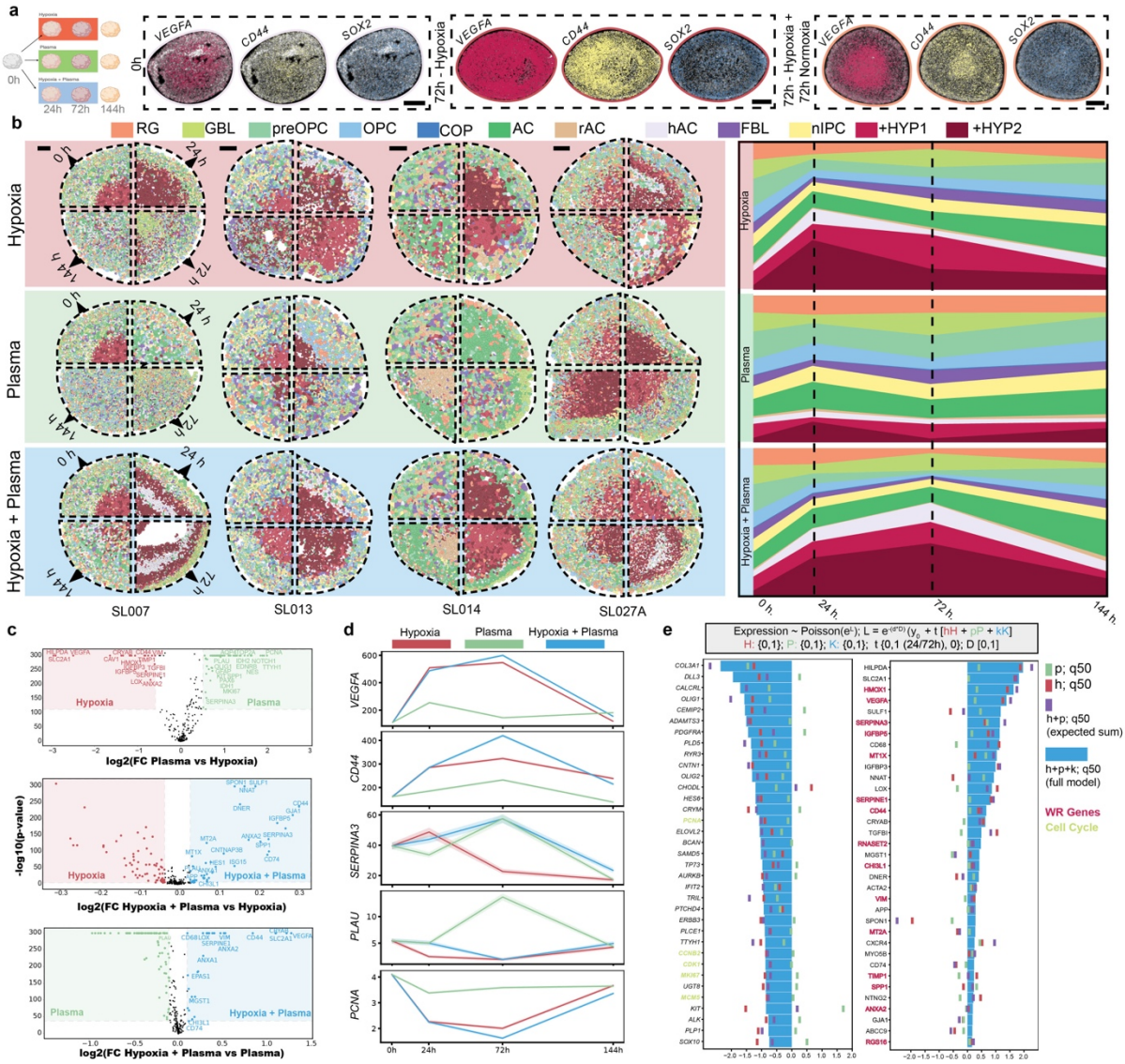

Figure 2. Transitional activation of WR program in patient-derived organoid lines. a, Left: schema of experiment. Right: expression of *SOX2*, *CD44* and *VEGFA* in organoid line SL027A over the course of experiment. Scale bar 200 µm. **b**, Left: spatial cell state distribution clocks of RG-, GBL-, preOPC-, OPC-, committed oligodendrocyte precursor (COP)-, AC-, reactive astrocyte (rAC)-, hypoxic astrocyte (hAC)-, FBL- and nIPC-like, +HYP1 and +HYP1 states at 0, 24, 72 and 144 hours when cultured under hypoxia, blood plasma or both. Scale bar (100 µm) corresponds to the top left quadrant (0 h timepoint), other quadrants are scaled to match the display size of the top left quadrant. Right: corresponding cell state proportions. **c**, Pairwise differential gene expression analysis between the different culturing conditions. **d**, Normalized expression of differentially expressed genes under different culturing conditions: *VEGFA*, *CD44, SERPINA3, PLAU* and *PCNA.* **e**, Top box: generalized linear model of gene expression according to a Poisson distribution with parameters: treatment timepoint (t), hypoxia (h), plasma (p), hypoxia and plasma (k), relative distance to organoid core (d). Left: genes with lowest effect size for k. Right: genes with highest effect size for combined treatment (k). Green line: estimated median from the posterior distribution for plasma effect size (p). Red line: estimated median from the posterior distribution for hypoxia effect size (h). Purple line: sum of hypoxia and plasma estimated medians. Blue bar: estimated median for the interaction effect between hypoxia and plasma (k). Cell cycle genes (green), wound response genes (red).

319 The glia-like states appeared spatially disorganized, whereas +HYP1 and +HYP2 states were
320 localized in the center of the GBOs (**Fig. 2b**: left), as could be expected given an oxygen
321 diffusion gradient along the surface-to-core axis. Both hypoxic programs were upregulated
322 under hypoxia, reverting to starting levels upon return to normoxia (**Fig. 2b)**, whereas the glial
323 marker *SOX2* maintained much more stable expression (**Fig 2a**). No pronounced changes in
324 cell state proportion were associated with plasma exposure alone, and the effects of the
325 combined hypoxia and plasma exposure paralleled those of hypoxia (**Fig. 2b**: right**)**.
326 Differential gene expression analysis of hypoxia and plasma treatments showed that hypoxia
327 upregulated conventional MES-like genes (*ANXA2*, *CD44*, *HILPDA*, *VEGFA*, among others),
328 whereas a more varied transcriptional signature was associated with plasma, including markers
329 of proliferation (*PCNA*, *MKI67*, *TOP2A*), glial markers (*AQP4*, *GFAP*, *NOTCH1*, *NES*,
330 *EDNRB*, *PAX6*), reactive gliosis marker *SERPINA3* and plasminogen activator *PLAU* (**Fig. 2c**:
331 top). To account for inhibitory effects and synergistic interactions, we next compared the two
332 individual culturing conditions to the combined one (**Fig. 2c**). Genes upregulated under
333 combined exposure to plasma and hypoxia as compared to hypoxia alone included
334 neurodevelopmental genes (*DNER, SPON1, SULF1, NNAT*), conventional MES-like markers
335 (*ANXA1*, *CHI3L1*, *MT1X*, *MT2A*) and immune response-related genes (*SPP1*, *CD74*; **Fig 2c**:
336 middle). Several of these (*ANXA1/2*, *CD44*, *CHI3L1*) were also upregulated in the combination
337 treatment as compared to plasma treatment (**Fig 2c**: bottom), indicating a synergistic effect of
338 hypoxia and plasma. Indeed, while for some genes the combined effect matched that of hypoxia
339 (*VEGFA*, *PLAU, PCNA*) or plasma (*SERPINA3*) alone, others (*CD44*) responded to each
340 condition differently (**Fig. 2d**).

341 To estimate the respective effect size of every factor on gene expression, we fit a Poisson
342 regression model (**Fig. 2e**: top, **Extended Data Fig. 8c**). The combined hypoxia and plasma
343 treatment upregulated multiple WR genes, and more strongly so than either condition alone
344 (**Fig. 2e**: right). Conversely, cell cycle markers were among the most downregulated under
345 combined treatment, although this effect was largely attributable to hypoxia alone (**Fig. 2e**:
346 left). Curiously, in many instances, the true combined effect of hypoxia and plasma did not
347 match the expected sum of effect sizes of each individual factor (*HILPDA*, *TGFBI*) or even
348 opposed the expected sum effect (*SPON1, CD74, MGST1, MT2A, GJA1*, *ABCC9*). Taken
349 together, these data show that a wound-like environment of hypoxia and blood plasma leads to
350 a transient induction of WR signatures in tumor cells, supporting the reactive and modular
351 nature of WR states in GBM.

352 **Vasculature is an organizing hub for wound response states**

353 We next examined whether this reactive model of WR states could likewise help explain their
354 organization in tumor context. We noticed that many tumors in our EEL-FISH dataset
355 displayed a sharp structural dichotomy between WR regions and more peripheral areas
356 containing non-WR tumor cells, astrocytes and oligodendrocytes (**Fig. 3a**). This distinction
357 likely reflects the transition from the high- to the low-fluorescence zone described previously
358 in the scRNA-seq data. Within the WR-rich zones, WR m-states were generally nested around
359 blood vessels: an *MGP*$^{+}$ WR m-state was associated with endothelial and mural cells (hence
360 annotated as WR Endothelial Associated), *VEGFA*-high WR m-states (WR OPC, WR nIPC
361 and WR HYP1/2) were located distally in respect to vasculature, and WR Periphery 1/2/3 m-
362 states spread out from vessels to periphery (**Fig. 3a**: Ia,b, **Extended Data Fig. 7d**).

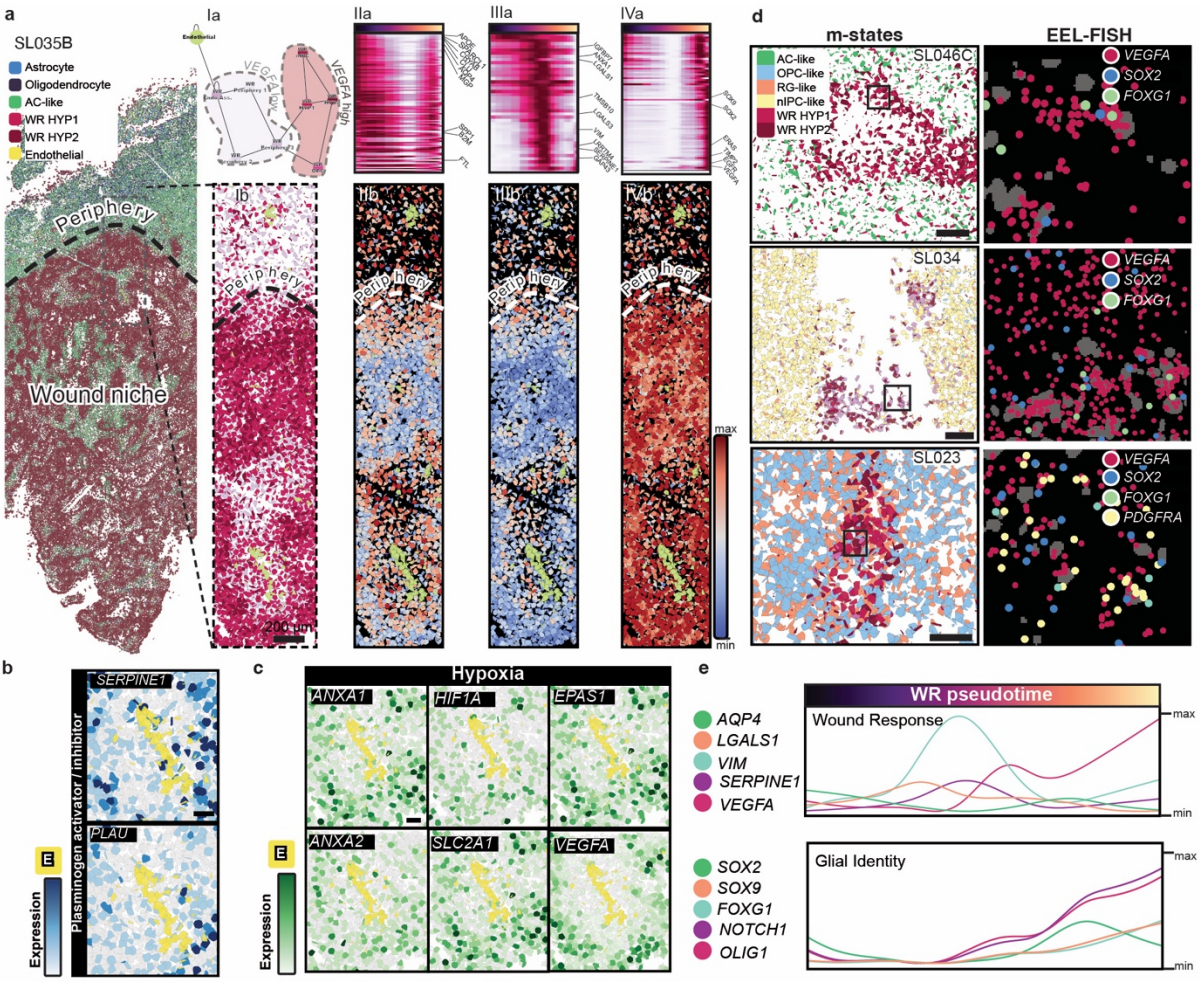

363

364 **Figure 3. Activation of WR program in GBM. a**, Left: spatial distribution of astrocytes,
365 oligodendrocytes, AC-like, WR HYP1/2 and endothelial m-states in sample SL035B. Ia: Graph
366 representation of spatial relationships between WR states and endothelial cells. Ib: Spatial distribution
367 of WR and endothelial m-cells across peripheral, wound and perivascular niches in sample SL035B.
368 IIa: peripheral/perivascular WR gene module expression along WR pseudotime; IIb: spatial distribution
369 of the peripheral/perivascular WR gene module. IIIa: intermediate WR gene module expression along
370 WR pseudotime; IIIb: spatial distribution of the intermediate WR gene module. IVa: wound niche WR
371 gene module expression along WR pseudotime; IVb: spatial distribution of the wound niche WR gene
372 module. **b**, Expression of *SERPINE1* and *PLAU* in the perivascular niche. Endothelial cells marked in
373 yellow. **c**, Expression of *ANXA1/2*, *HIF1A*, *EPAS1*, *SLC2A1* and *VEGFA* in the perivascular niche.
374 Endothelial cells marked in yellow. **d**, Spatial distribution of AC-like, OPC-like, RG-like, nIPC-like and
375 WR HYP1/2 m-states in samples SL046C, SL034 and SL023. EEL-FISH co-expression for *VEGFA*,
376 *SOX2*, *FOXG1* and *PDGFRA* in WR cells. **e**, WR pseudotime normalized expression of wound response
377 (*AQP4*, *LGALS1*, *VIM*, *SERPINE1* and *VEGFA*) and glial (*SOX2*, *SOX9*, *FOXG1*, *NOTCH1* and *OLIG1*)
378 genes.

379 We used scFates[50] to fit a pseudotime trajectory along these m-states and observed a
380 progression reflective of the spatial organization (**Extended Data Fig. 7d**). Namely, the wound
381 response trajectory ranged from the less hypoxic WR m-states of the peripheral tumor regions
382 (**Fig. 3a**: I, **Extended Data Fig. 7d**: SL002) to m-states with the highest *VEGFA* expression
383 (WR HYP1/2), located farthest away from vasculature (**Fig. 3a**: I, **Extended Data Fig. 7d**:
384 SL035B). We organized this WR state gradient into three gene modules that respectively
385 defined the peripheral/perivascular (**Fig. 3a**: II), intermediate (**Fig. 3a**: III) and hypoxic states
386 (**Fig. 3a**: IV). Notable hypoxia response genes (*ANXA1/2*, *HIF1A*, *SLC2A1*, *EPAS1*, *VEGFA*),

signaling molecules *(NOTCH1, TGFBI, IGFBP5)*, and hemostasis regulators (*SERPINE1*, *PLAU*) followed a vasculature-centered gradient (**Fig. 3b,c**, **Extended Data Fig. 7e**), analogously to the surface-to-core axis in our GBO models. The structured transcriptional organization around vessels suggests that akin to *in vitro* induction in GBOs, WR states could be governed by tumor hypoxia gradients. In line with the reactive state hypothesis, we also found that WR m-cells maintained the expression of key glial markers (*SOX2*, *FOXG1* or *PDGFRA*) across tumors of distinct characteristic glia-like cell compositions (**Fig. 3d**). Expression of some glial factors (*SOX2*, *SOX9*, *FOXG1, OLIG1*, *NOTCH1*) even increased along the WR pseudotime axis (**Fig. 3e**). Thus, we conclude that WR activation does not negate glia-like identity of tumor cells and that the level of activation depends primarily on local hypoxia gradients, in line with recent reports identifying hypoxia as an organizing factor in GBM[51].

Hypoxia links immune infiltration to wound response microenvironment

We next asked what other cellular components contributed to the wound response microenvironment. Firstly, we found a particularly strong and widespread spatial association between hypoxic tumor WR m-cells (WR HYP), monocytes (Mono1 and Mono2) and hypoxic moTAMs (moTAM HYP, *SPP1*$^{+}$*MT1H*$^{+}$; **Fig. 4a**: I). Conversely, non-hypoxic moTAMs and mgTAMs were associated with peripheral WR and non-WR tumor m-cells, alongside non-malignant astrocytes and oligodendrocytes (**Fig. 4a**: I).

To investigate how this immune-WR niche could be established, we selected four samples ranging from low to high WR content, thereby approximating a time series of the niche construction (**Fig. 4a**: II). The association between infiltrating monocytes (Mono1), moTAM HYP and tumor WR m-cells was maintained regardless of WR level (**Fig. 4b**). Notably, even in the most WR-rich samples, perivascular niches were not overridden by WR (**Fig. 4a**: III). Conversely, even in extremely low-WR tumors, we found areas of high expression of both the pro-inflammatory *IL1B* and the hypoxic *SPP1* (**Fig. 4c**: SL001B). These areas were infiltrated by monocytes (**Fig. 4c**: IIa), particularly in the more hypoxic pockets, as marked by high *HMOX1* expression (**Fig. 4c**: IIb), possibly reflecting an early stage of the immune-WR niche progression. Similar, but more advanced patterns were observed in tumors with higher WR content, where monocytes were mixed with moTAMs and surrounded by WR HYP m-cells (**Fig. 4c**: SL046C). Within the hypoxic pockets of monocytes, we located m-cells expressing interferon-related genes *IFIT2, IFIT3, ISG15* and *IL1B* (**Fig. 4c**: III,IV), similar to the previously reported signature of CD16^{-} monocytes[52]. In samples with high WR content, WR niches were far more scarcely infiltrated by monocytes, with similar levels of moTAM HYP instead (**Fig. 4c**: SL061B and SL035B). We believe that these data might indeed capture the gradual progression of WR niches, beginning with monocyte recruitment to hypoxic areas (*HMOX1*$^{+}$) and a concurrent switch towards WR states in tumor cells, whereupon monocytes remain sequestered among WR tumor cells, differentiating into immunosuppressive macrophages (*CD74*$^{+}$*CD163*$^{+}$*TREM2*$^{+}$) with a hypoxic signature (**Fig. 4c**: V). Such a sequence of events would be in line with the reports showing that hypoxic niches attract and sequester TAMs, ultimately leading to pseudopalisade formation[53].

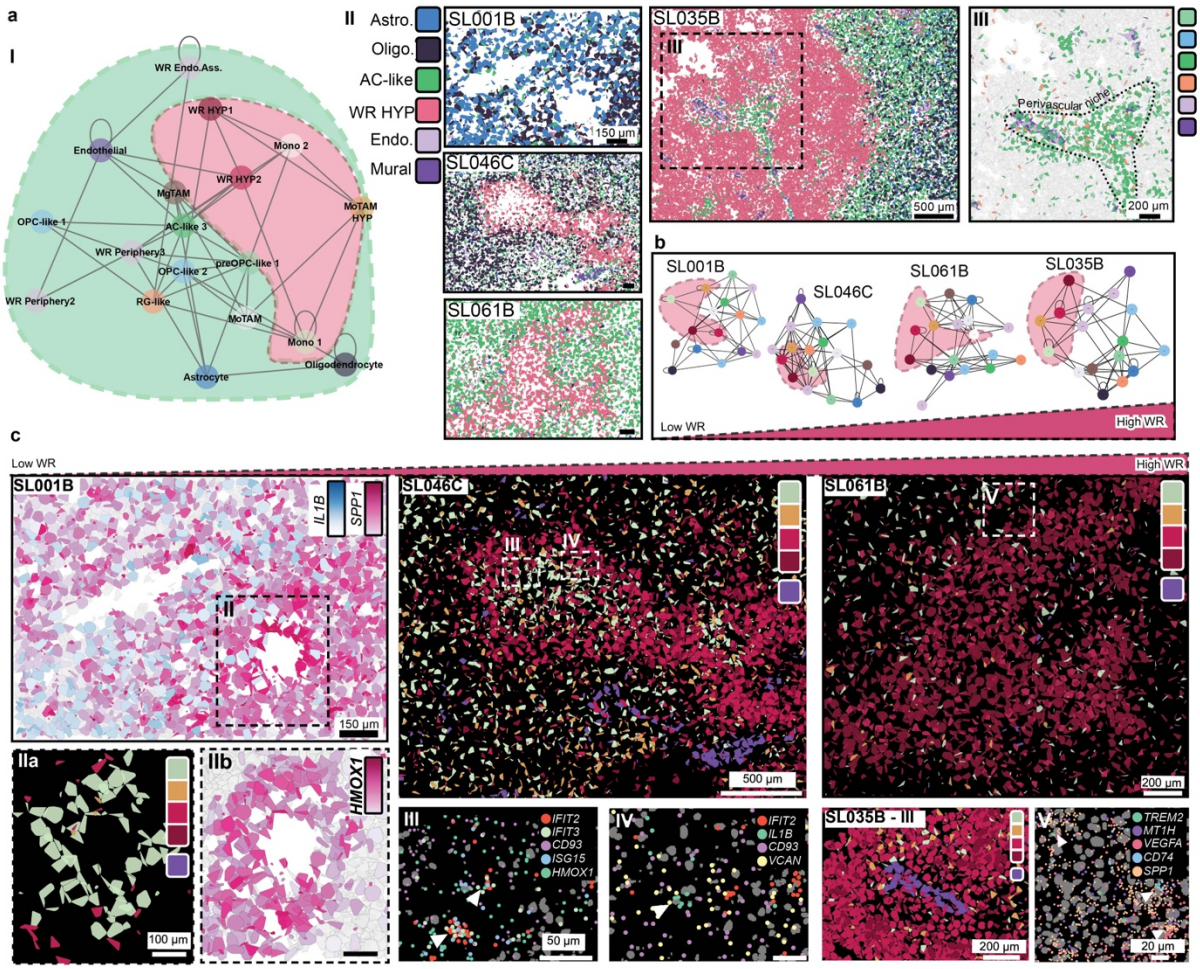

Figure 4. Immune infiltration of the WR niche in GBM. a, I: Spatial connectivity graph of GBM m-states across all samples. Edges indicate significant connections. Immune-WR niche highlighted in red. II: Spatial distribution of astrocyte, oligodendrocyte, AC-like, WR HYP, endothelial and mural m-states in samples SL001B, SL046C, SL061B and SL035B. III: spatial distribution of m-states in a perivascular niche in sample SL035B. Color legend matches panel I. **b**, Spatial connectivity graph of m-states in samples SL001B, SL046C, SL061B and SL035B. **c**, Left: IL1B and SPP1 expression in sample SL001B (top). IIa: Spatial distribution of monocyte, moTAM HYP, WR HYP, endothelial and mural m-states in sample SL001B. IIb: HMOX1 expression in monocyte infiltrating region of sample SL001B. Middle: spatial distribution of monocyte, moTAM HYP, WR HYP, endothelial and mural m-states in sample SL046C (top). III and IV: IFIT2/3, IL1B and ISG15 expression in hypoxic (HMOX1) and monocyte infiltrating (CD93/VCAN) regions of sample SL046C. Right: spatial distribution of monocyte, moTAM HYP, WR HYP, endothelial and mural m-states in samples SL061B and SL035B. V: anti-inflammatory (TREM2) and hypoxia signatures (SPP1, MT1H, VEGFA) in moTAM HYP infiltrating (CD74+) region of sample SL061B. M-state color legends match panel **a**(I).

Wound response-independent spatial organization is conserved across patients

We lastly searched for universal spatial GBM characteristics conserved between patients. Matching mutational profiles often corresponded to spatial profile similarity but the most striking division was found between WR-low and WR-high samples (**Fig. 5a**). The stratification by WR activation was observed even within a sample originating from the same patient (e.g., SL046B/C) suggesting that local WR effects, rather than mutational predispositions, dominate tumor niche architecture. We reevaluated spatial associations by excluding WR m-states to eliminate potential masking effects (**Fig. 5b**). AC-like 3 (*CRYAB*$^{+}$) m-state was recurrently found near endothelial and mural cells (**Fig. 5b,c**, **Extended Data Fig.**

9), similarly to the well-documented colocalization of healthy mature astrocytes with vasculature[54]. We observed this association across tumors of varied WR proportions and mutation profiles (**Fig. 5c**: SL035B, SL034 and SL046B/C). Similarly, we observed a consistent association between preOPC-like 1 and OPC-like 2 m-cells (**Fig. 5b,c**). The spatial association between the supposed precursor-descendant state pair supports our classification of this *EGFR*$^{+}$ m-state as preOPC-like. Taken together, these data suggest that the basic GBM organization, upon which WR activation is superimposed, retains features characteristic of its tissue of origin, the brain.

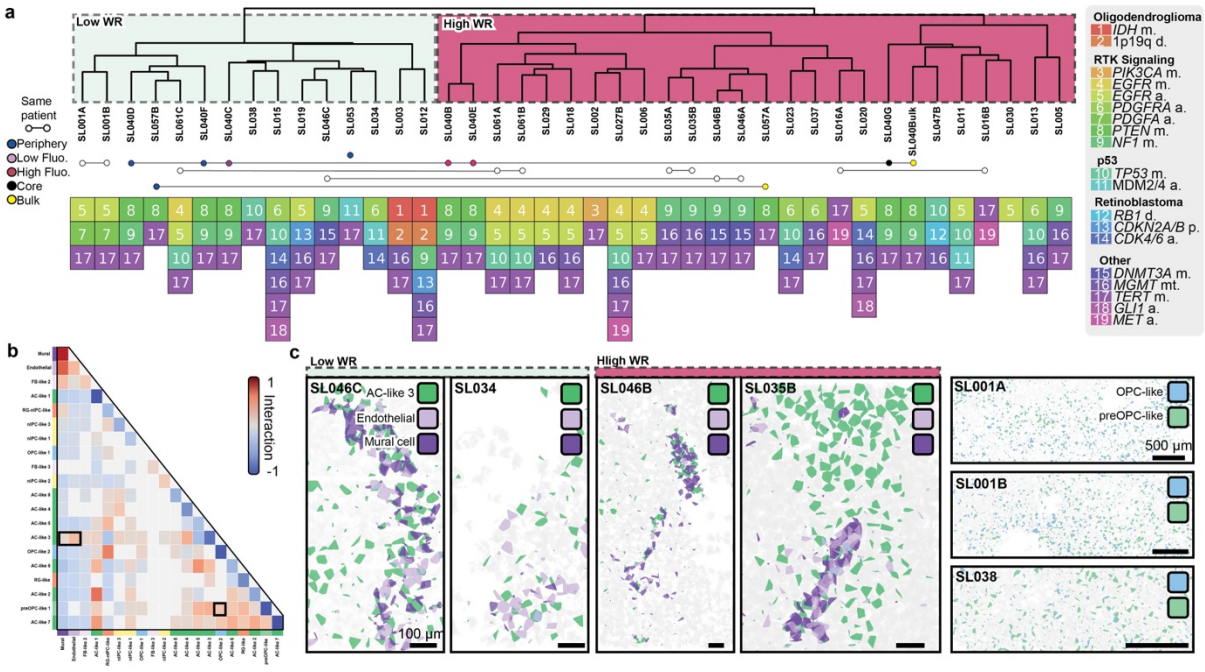

Figure 5. Spatial organization of cell states across a large GBM cohort. a, Dendrogram of m-state spatial organization similarity across samples with corresponding mutational profiles. Connected dots mark samples originating from one patient, color-coded by sampling location. Each square indicates mutations identified in the pathology report (Supplementary Table 3): mutated (m.), amplified (a.), deleted (d.), positive signal (p.), methylated (mt.). **b**, Neighborhood enrichment scores for non-WR tumor, endothelial and mural m-states in all samples. **c**, Spatial distribution of AC-like 3, endothelial and mural m- samples SL034, SL035, SL046B/C. Spatial distribution of OPC-like 2 and preOPC-like 1 m-states in samples SL001A/B and SL038. Gray polygons represent all other m-states.

Discussion

Our understanding of GBM has been largely built on data acquired from the contrast-enhancing zone of the tumor bulk, as determined by the current clinical practices of maximal safe resection. By studying rare cases where tissue from tumor periphery was also accessible, we showed that the molecular architecture changes drastically along the core-to-periphery axis. The tumor bulk was dominated by a hypoxia and wound response program shared across malignant and non-malignant cell types and an abundance of TAMs. In contrast, the low-fluorescence zone just outside the tumor bulk showed very little wound response and contained normal glia and lack of TAMs despite considerable infiltration by proliferative tumor cells. We believe that the emergence of WR states in the tumor bulk may reflect a fundamental self-perpetuating mechanism in GBM (**Extended Data Fig. 10**): a growing tumor causes tissue damage, vascular dysfunction and oxygen depletion, inducing hypoxia and clotting that activate WR states, which, through secreted factors such as *VEGFA*, further increase vascular

483 leakage and thus reinforce WR activation in a cycle of futile wound response[55]. Monocytes
484 recruited to this unresolvable wound niche would ultimately differentiate towards WR-
485 signature expressing moTAMs and further contribute to the wound-like environment.
486 Metabolic factors, like high oxygen consumption by myeloid cells[56] could further reinforce the
487 vicious cycle. While intrinsic factors, namely *NF1* alterations, have been linked to the MES-
488 like state[1,5], our multi-region sample SL040 lacked MES-like signature expression outside of
489 the tumor bulk despite carrying a clinically confirmed *NF1*-mutation (**Supplementary**
490 **Table 3**), showing that *NF1* alterations were insufficient to intrinsically induce MES-like states
491 outside of their requisite spatial context. This re-interpretation of MES-like (*i.e.*, WR)
492 phenotypes not as tumor-intrinsic but rather as tissue-wide reactive states driven by rapid tumor
493 growth would imply that these cell states are a consequence of tumor aggressiveness, not its
494 cause.

495 Importantly, such chronic and hypoxic wound response mechanisms might not be GBM-
496 specific: multiple studies in solid tumors have shown that hypoxic gene signatures are
497 prognostic markers of an aggressive disease with a short survival[57–60]. Five of the top 15 genes
498 in the shortlist from various solid tumors by Buffa *et al.*[58] are part of the MES-like signature
499 (S*LC2A1, LDHA, P4HA1, ADM, NDRG1*), and another six are present in our WR signature
500 (Supplementary table 2). Of the 15 genes shortlisted in pancreatic cancer by Khouzam *et al.*[60],
501 nine are part of the MES-signature (*NDRG1, SLC2A1, P4HA1, LDHA, PGK1, ANGPTL,*
502 *BNIP3, ADM, CA9*).

503 In summary, our findings show that the WR signature is cell-extrinsic, confined to the bulk of
504 the tumor and shared across tumor and non-tumor cell types. Given our findings of WR
505 activation as a strong central and universal feature of GBM, other recent reports highlighting
506 the role of injury-like processes in GBM progression[61] and the suspected relevance of WR in
507 other solid tumors, the reconceptualization of MES-like cell states as WR is not a simple
508 refinement of nomenclature but a shift in perspective regarding the interplay between tumor
509 cell type, state and tissue organization. Recognizing WR as a modular tissue state should spark
510 renewed interest in the truly tumor-intrinsic malignant cell types and the unique
511 microenvironment outside the tumor bulk, the probable source of most relapses in GBM.

512 **REFERENCES**

513 1. Verhaak, R. G. W. *et al.* Integrated Genomic Analysis Identifies Clinically Relevant
514 Subtypes of Glioblastoma Characterized by Abnormalities in PDGFRA, IDH1, EGFR, and
515 NF1. *Cancer Cell* **17**, 98–110 (2010).
516 2. Patel, A. P. *et al.* Single-cell RNA-seq highlights intratumoral heterogeneity in primary
517 glioblastoma. *Science* **344**, 1396–1401 (2014).
518 3. Tirosh, I. *et al.* Single-cell RNA-seq supports a developmental hierarchy in human
519 oligodendroglioma. *Nature* **539**, 309–313 (2016).
520 4. Venteicher, A. S. *et al.* Decoupling genetics, lineages, and microenvironment in IDH-
521 mutant gliomas by single-cell RNA-seq. *Science* **355**, eaai8478 (2017).
522 5. Neftel, C. *et al.* An Integrative Model of Cellular States, Plasticity, and Genetics for
523 Glioblastoma. *Cell* **178**, 835-849.e21 (2019).
524 6. Bhaduri, A. *et al.* Outer Radial Glia-like Cancer Stem Cells Contribute to Heterogeneity of
525 Glioblastoma. *Cell Stem Cell* **26**, 48-63.e6 (2020).
526 7. Couturier, C. P. *et al.* Single-cell RNA-seq reveals that glioblastoma recapitulates a normal
527 neurodevelopmental hierarchy. *Nat Commun* **11**, 3406 (2020).

528 8. Phillips, H. S. *et al.* Molecular subclasses of high-grade glioma predict prognosis, delineate
529 a pattern of disease progression, and resemble stages in neurogenesis. *Cancer Cell* **9**, 157–
530 173 (2006).
531 9. Hoogstrate, Y. *et al.* Transcriptome analysis reveals tumor microenvironment changes in
532 glioblastoma. *Cancer Cell* **41**, 678-692.e7 (2023).
533 10. Mahabir, R. *et al.* Sustained elevation of Snail promotes glial-mesenchymal transition after
534 irradiation in malignant glioma. *Neuro-Oncology* **16**, 671–685 (2014).
535 11. Segerman, A. *et al.* Clonal Variation in Drug and Radiation Response among Glioma-
536 Initiating Cells Is Linked to Proneural-Mesenchymal Transition. *Cell Reports* **17**, 2994–
537 3009 (2016).
538 12. Borm, L. E. *et al.* Scalable in situ single-cell profiling by electrophoretic capture of mRNA
539 using EEL FISH. *Nat Biotechnol* (2022) doi:10.1038/s41587-022-01455-3.
540 13. Ostrom, Q. T. *et al.* CBTRUS Statistical Report: Primary Brain and Other Central Nervous
541 System Tumors Diagnosed in the United States in 2016—2020. *Neuro-Oncology* **25**, iv1–
542 iv99 (2023).
543 14. Richards, L. M. *et al.* Gradient of Developmental and Injury Response transcriptional states
544 defines functional vulnerabilities underpinning glioblastoma heterogeneity. *Nat Cancer* **2**,
545 157–173 (2021).
546 15. Schmitt, M. J. *et al.* Phenotypic Mapping of Pathologic Cross-Talk between Glioblastoma
547 and Innate Immune Cells by Synthetic Genetic Tracing. *Cancer Discovery* **11**, 754–777
548 (2021).
549 16. Hart, W. S., Myers, P. J., Purow, B. W. & Lazzara, M. J. Divergent transcriptomic
550 signatures from putative mesenchymal stimuli in glioblastoma cells. *Cancer Gene Ther* **31**,
551 851–860 (2024).
552 17. Bhat, K. P. L. *et al.* The transcriptional coactivator TAZ regulates mesenchymal
553 differentiation in malignant glioma. *Genes Dev.* **25**, 2594–2609 (2011).
554 18. Bhat, K. P. L. *et al.* Mesenchymal Differentiation Mediated by NF-κB Promotes Radiation
555 Resistance in Glioblastoma. *Cancer Cell* **24**, 331–346 (2013).
556 19. Lau, J. *et al.* STAT3 Blockade Inhibits Radiation-Induced Malignant Progression in
557 Glioma. *Cancer Research* **75**, 4302–4311 (2015).
558 20. Hara, T. *et al.* Interactions between cancer cells and immune cells drive transitions to
559 mesenchymal-like states in glioblastoma. *Cancer Cell* **39**, 779-792.e11 (2021).
560 21. Pyonteck, S. M. *et al.* CSF-1R inhibition alters macrophage polarization and blocks glioma
561 progression. *Nat Med* **19**, 1264–1272 (2013).
562 22. Stafford, J. H. *et al.* Colony stimulating factor 1 receptor inhibition delays recurrence of
563 glioblastoma after radiation by altering myeloid cell recruitment and polarization. *Neuro*
564 *Oncol* **18**, 797–806 (2016).
565 23. Akkari, L. *et al.* Dynamic changes in glioma macrophage populations after radiotherapy
566 reveal CSF-1R inhibition as a strategy to overcome resistance. *Sci. Transl. Med.* **12**,
567 eaaw7843 (2020).
568 24. Chipman, M. E. *et al.* Tumor progression is independent of tumor-associated macrophages
569 in cell lineage–based mouse models of glioblastoma. *Proc. Natl. Acad. Sci. U.S.A.* **120**,
570 e2222084120 (2023).
571 25. Galarneau, H., Villeneuve, J., Gowing, G., Julien, J.-P. & Vallières, L. Increased Glioma
572 Growth in Mice Depleted of Macrophages. *Cancer Research* **67**, 8874–8881 (2007).
573 26. Yamahara, T. *et al.* Morphological and flow cytometric analysis of cell infiltration in
574 glioblastoma: a comparison of autopsy brain and neuroimaging. *Brain Tumor Pathol* **27**,
575 81–87 (2010).
576 27. Darmanis, S. *et al.* Single-Cell RNA-Seq Analysis of Infiltrating Neoplastic Cells at the
577 Migrating Front of Human Glioblastoma. *Cell Reports* **21**, 1399–1410 (2017).

28. Xie, Y. *et al.* Key molecular alterations in endothelial cells in human glioblastoma uncovered through single-cell RNA sequencing. *JCI Insight* (2021).
29. Stummer, W. *et al.* Fluorescence-guided surgery with 5-aminolevulinic acid for resection of malignant glioma: a randomised controlled multicentre phase III trial. *The Lancet Oncology* **7**, 392–401 (2006).
30. infercnvpy. https://github.com/icbi-lab/infercnvpy.
31. Sankowski, R. *et al.* Multiomic spatial landscape of innate immune cells at human central nervous system borders. *Nat Med* **30**, 186–198 (2024).
32. Mansouri, A., Lai, C., Scales, D. & Pirouzmand, F. A phase II pilot randomized controlled trial to assess the feasibility of the "supra-marginal" surgical resection of malignant glioma (G-SUMIT: Glioma supra marginal incision trial) study protocol. *Pilot Feasibility Stud* **8**, 138 (2022).
33. Gerritsen, J. K. W. *et al.* SUPRAMAX-study: supramaximal resection versus maximal resection for glioblastoma patients: study protocol for an international multicentre prospective cohort study (ENCRAM 2201). *BMJ Open* **14**, e082274 (2024).
34. Prabhu, A., Kesarwani, P., Kant, S., Graham, S. F. & Chinnaiyan, P. Histologically defined intratumoral sequencing uncovers evolutionary cues into conserved molecular events driving gliomagenesis. *Neuro-Oncology* **19**, 1599–1606 (2017).
35. Brooks, L. J., Simpson Ragdale, H., Hill, C. S., Clements, M. & Parrinello, S. Injury programs shape glioblastoma. *Trends in Neurosciences* **45**, 865–876 (2022).
36. St. Laurent, G. *et al.* Deep Sequencing Transcriptome Analysis of Murine Wound Healing: Effects of a Multicomponent, Multitarget Natural Product Therapy-Tr14. *Front. Mol. Biosci.* **4**, 57 (2017).
37. Chanoch-Myers, R., Wider, A., Suva, M. L. & Tirosh, I. Elucidating the diversity of malignant mesenchymal states in glioblastoma by integrative analysis. *Genome Med* **14**, 106 (2022).
38. Wei, H. *et al.* Systematic analysis of purified astrocytes after SCI unveils Zeb2os function during astrogliosis. *Cell Reports* **34**, 108721 (2021).
39. Garza, R. *et al.* Single-cell transcriptomics of human traumatic brain injury reveals activation of endogenous retroviruses in oligodendroglia. *Cell Reports* **42**, 113395 (2023).
40. Biancalani, T. *et al.* Deep learning and alignment of spatially resolved single-cell transcriptomes with Tangram. *Nat Methods* **18**, 1352–1362 (2021).
41. Ruiz-Moreno, C. *et al. Harmonized Single-Cell Landscape, Intercellular Crosstalk and Tumor Architecture of Glioblastoma*. http://biorxiv.org/lookup/doi/10.1101/2022.08.27.505439 (2022) doi:10.1101/2022.08.27.505439.
42. Braun, E. *et al.* Comprehensive cell atlas of the first-trimester developing human brain. *Science* **382**, eadf1226 (2023).
43. Huang, W. *et al.* Origins and Proliferative States of Human Oligodendrocyte Precursor Cells. *Cell* **182**, 594-608.e11 (2020).
44. Van Bruggen, D. *et al.* Developmental landscape of human forebrain at a single-cell level identifies early waves of oligodendrogenesis. *Developmental Cell* **57**, 1421-1436.e5 (2022).
45. Wang, L. *et al.* Molecular and cellular dynamics of the developing human neocortex. *Nature* (2025) doi:10.1038/s41586-024-08351-7.
46. Wang, L., Hou, S. & Han, Y.-G. Hedgehog signaling promotes basal progenitor expansion and the growth and folding of the neocortex. *Nat Neurosci* **19**, 888–896 (2016).
47. Liberzon, A. *et al.* The Molecular Signatures Database Hallmark Gene Set Collection. *Cell Systems* **1**, 417–425 (2015).
48. The Tabula Sapiens Consortium* *et al.* The Tabula Sapiens: A multiple-organ, single-cell transcriptomic atlas of humans. *Science* **376**, eabl4896 (2022).

49. Lopez, R., Regier, J., Cole, M. B., Jordan, M. I. & Yosef, N. Deep generative modeling for single-cell transcriptomics. *Nat Methods* **15**, 1053–1058 (2018).
50. Faure, L., Soldatov, R., Kharchenko, P. V. & Adameyko, I. scFates: a scalable python package for advanced pseudotime and bifurcation analysis from single-cell data. *Bioinformatics* **39**, btac746 (2023).
51. Greenwald, A. C. *et al.* Integrative spatial analysis reveals a multi-layered organization of glioblastoma. *Cell* **187**, 2485-2501.e26 (2024).
52. Mulder, K. *et al.* Cross-tissue single-cell landscape of human monocytes and macrophages in health and disease. *Immunity* **54**, 1883-1900.e5 (2021).
53. Sattiraju, A. *et al.* Hypoxic niches attract and sequester tumor-associated macrophages and cytotoxic T cells and reprogram them for immunosuppression. *Immunity* **56**, 1825-1843.e6 (2023).
54. Abbott, N. J., Rönnbäck, L. & Hansson, E. Astrocyte–endothelial interactions at the blood–brain barrier. *Nat Rev Neurosci* **7**, 41–53 (2006).
55. Dvorak, H. F. Tumors: Wounds That Do Not Heal—Redux. *Cancer Immunology Research* **3**, 1–11 (2015).
56. Mirchandani, A. S., Sanchez-Garcia, M. A. & Walmsley, S. R. How oxygenation shapes immune responses: emerging roles for physioxia and pathological hypoxia. *Nat Rev Immunol* (2024) doi:10.1038/s41577-024-01087-5.
57. Chi, J.-T. *et al.* Gene Expression Programs in Response to Hypoxia: Cell Type Specificity and Prognostic Significance in Human Cancers. *PLoS Med* **3**, e47 (2006).
58. Buffa, F. M., Harris, A. L., West, C. M. & Miller, C. J. Large meta-analysis of multiple cancers reveals a common, compact and highly prognostic hypoxia metagene. *Br J Cancer* **102**, 428–435 (2010).
59. Lin, W. *et al.* Characterization of Hypoxia Signature to Evaluate the Tumor Immune Microenvironment and Predict Prognosis in Glioma Groups. *Front. Oncol.* **10**, 796 (2020).
60. Abou Khouzam, R. *et al.* An Eight-Gene Hypoxia Signature Predicts Survival in Pancreatic Cancer and Is Associated With an Immunosuppressed Tumor Microenvironment. *Front. Immunol.* **12**, 680435 (2021).
61. Hamed, A. A. *et al.* Gliomagenesis mimics an injury response orchestrated by neural crest-like cells. *Nature* (2025) doi:10.1038/s41586-024-08356-2.
62. Gerard, I. J. *et al.* Brain shift in neuronavigation of brain tumors: A review. *Medical Image Analysis* **35**, 403–420 (2017).
63. Schucht, P. *et al.* 5-ALA complete resections go beyond MR contrast enhancement: shift corrected volumetric analysis of the extent of resection in surgery for glioblastoma. *Acta Neurochir* **156**, 305–312 (2014).
64. Korsunsky, I. *et al.* Fast, sensitive and accurate integration of single-cell data with Harmony. *Nat Methods* **16**, 1289–1296 (2019).
65. Wolf, F. A., Angerer, P. & Theis, F. J. SCANPY: large-scale single-cell gene expression data analysis. *Genome Biol* **19**, 15 (2018).
66. Moffitt, J. R. & Zhuang, X. RNA Imaging with Multiplexed Error-Robust Fluorescence In Situ Hybridization (MERFISH). in *Methods in Enzymology* vol. 572 1–49 (Elsevier, 2016).
67. Kvedaraite, E. *et al.* Notch-dependent cooperativity between myeloid lineages promotes Langerhans cell histiocytosis pathology. *Sci. Immunol.* **7**, eadd3330 (2022).
68. Jacob, F., Ming, G. & Song, H. Generation and biobanking of patient-derived glioblastoma organoids and their application in CAR T cell testing. *Nat Protoc* **15**, 4000–4033 (2020).
69. Stringer, C., Wang, T., Michaelos, M. & Pachitariu, M. Cellpose: a generalist algorithm for cellular segmentation. *Nat Methods* **18**, 100–106 (2021).
70. Rocklin, M. Dask: Parallel computation with blocked algorithms and task scheduling. in *Proceedings of the 14th Python in Science Conference* 126–132 (2015).

71. Partel, G. & Wählby, C. Spage2vec: Unsupervised representation of localized spatial gene expression signatures. *The FEBS Journal* **288**, 1859–1870 (2021).
72. Hamilton, W. L., Ying, R. & Leskovec, J. Inductive Representation Learning on Large Graphs. in *31st Conference on Neural Information Processing Systems* (2017).
73. Brody, S., Alon, U. & Yahav, E. How attentive are graph attention networks? in *International Conference for Learning Representations* (2022).
74. Kingma, D. P. & Ba, J. Adam: A Method for Stochastic Optimization. in *International Conference for Learning Representations* (2015).
75. Domínguez Conde, C. *et al.* Cross-tissue immune cell analysis reveals tissue-specific features in humans. *Science* **376**, eabl5197 (2022).
76. Abril-Pla, O. *et al.* PyMC: a modern, and comprehensive probabilistic programming framework in Python. *PeerJ Computer Science* **9**, e1516 (2023).
77. Palla, G. *et al.* Squidpy: a scalable framework for spatial omics analysis. *Nat Methods* **19**, 171–178 (2022).
78. Pham, D. *et al.* Robust mapping of spatiotemporal trajectories and cell–cell interactions in healthy and diseased tissues. *Nat Commun* **14**, 7739 (2023).

METHODS

Patient samples

Human glioblastoma samples were collected with informed consent from the patients and with ethical approval from the Swedish Ethical Review Authority (2020-03505). The use of samples was approved by the Swedish Ethical Review Authority (2020-02096). Information on clinical metadata and neuropathology data can be found in Supplementary Table 3.

Human tissue collection

GBM samples were kept fresh in Hibernate-E medium (Gibco) on ice during transportation from neurosurgery at the Karolinska University Hospital. Upon arrival, samples were either directly processed for scRNA-seq or embedded in Tissue-Tek Optimal Cutting Temperature (O.C.T.; Sakura) compound and snap-frozen in 2-methylbutane (Sigma Aldrich) and dry ice slurry. Frozen samples were stored at −80°C until further use.

Multi-region sampling rationale

Neuronavigation, using preoperative MRI, was used according to standard of care. This is a central tool used on a regular basis in surgery of GBM. However, brain shift is a notorious and frequent problem and increasingly so during the continuous surgical removal of the tumor[62]. This compromises the accuracy of biopsies, especially when sampling from multiple locations. The fluorescence from 5-ALA, on the other hand, corresponds very well with the contrast-enhancing zone and extends beyond its outer margin, enabling an intraoperative delineation and guidance for the neurosurgeon[63]. Sampling based on 5-ALA fluorescence eliminates brain shift bias and we therefore decided to define the location of the biopsies based on the fluorescence rather than neuronavigation alone. Systematic sampling was done at multiple distances from the center of the tumor core in four different directions (anterior, posterior, superior, inferior) using a biopsy rongeur yielding approximately 3x5 mm tissue biopsies from each location. Sampling was performed early in the resection procedure to minimize brain shift, and each sample individually analyzed under blue light to define fluorescence intensity.

Tissue dissociation

First, the tissue was chopped into small pieces using a razor blade. The Worthington's Papain Dissociation System (Worthington) was used for enzymatic digestion at 37°C for 15-40 min (depending on the region, cortical samples usually required longer time). Manual trituration of

725 the suspension was performed with glass pipettes. The suspension was subsequently filtered
726 through a 70-µm filter followed by a 30-µm filter (Miltenyi, CellTrics). After centrifugation
727 (200 g for 5 min at 4-8°C) the pellet was resuspended in EBSS (Worthington). Gradient
728 centrifugation was performed using an albumin inhibitor solution (Worthington), followed by
729 lysis of erythrocytes with RBC lysis buffer (Invitrogen) according to the manufacturer's
730 instructions. After final resuspension in EBSS visual inspection was done on a hemocytometer
731 to estimate viability of the suspension (1 part Trypan blue 0.4%, Gibco, and 1 part cell
732 suspension) and confirm minimal presence of multiplets, debris and to estimate the
733 concentration of cells.

734 ***Single-cell RNA sequencing***
735 We processed two to three replicates per sample with the 10X Genomics V3.1 kits. If needed,
736 dilution or resuspension was performed to reach a concentration corresponding to a target of
737 about 10,000 cells per replicate when loading on the 10X Genomics chromium chips. Shallow
738 sequencing (about 1000 reads per cell, Illumina NextSeq platform) was performed for quality
739 control and estimate of cell concentrations followed by deep sequencing of about 100,000 reads
740 per cell on the Illumina NovasSeq platform.

741 Sequencing runs were demultiplexed, filtered through an index-hopping filter, UMIs were
742 counted and reads aligned to a human reference genome as previously described[42].

743 ***Single-cell RNA sequencing quality control***
744 Broken 10X chromium emulsions were discarded. After library preparation, the cDNA yield
745 and fragment distribution were evaluated (2100 Bioanalyzer Instrument, Agilent
746 Technologies). Replicates with more than 25,000 cells after deep sequencing were not analyzed
747 further. Droplet classification was based on a previously described approach[42]; thresholds were
748 modified based on evaluating the droplet distribution (UMI vs unspliced read fraction) with
749 the final criteria: minimum UMI count of 4000, minimum unspliced read fraction of 0.1,
750 maximum doublet score of 0.4, maximum mitochondrial read fraction of 0.25, two-
751 dimensional Gaussian maximum likelihood values m=30, k=1500.

752 ***Single-cell RNA sequencing data analysis***
753 Data were analyzed using Cytograph-Shoji (https://github.com/linnarsson-lab/cytograph-
754 shoji), which implements a custom tensor database. All cells that passed our QC criteria were
755 clustered as previously described[42] but with 2000 most variable genes (instead of 1000)
756 selected using support-vector regression on the CV-versus-mean relationship. Harmony[64] was
757 not required since only one 10X chemistry version was used.

758 ***Single-cell annotation***
759 Manual curation was performed based on multiple established cell type-specific markers. Cells
760 with combined expression of genes specific to more than one cell type were suspected to be
761 doublets and were filtered out. After this step, re-clustering and re-annotation was performed.
762 For distinction within the myeloid populations the following genes were used. mgTAMs shared
763 expression of microglia genes (*CX3CR1, P2RY12, P2RY13, TMEM119*) as well as moTAM
764 genes (*F13A1, S100A8, S100A9*) which were absent in microglia. For mgTAMs *HAMP* was
765 specific. Microglia was the only cell type expressing the dendritic cell markers *CLEC9A* and
766 *FCER1A*. Genes present in both macrophages and moTAMs were *ITGA4, RNASE1, F13A1* but
767 macrophages lacked TAM genes (*S100A8, S100A9, SPP1, VCAN)* and *EREG,* a gene specific
768 for a subset of moTAMs.

769 ***Inferring CNVs in single cells***

770 We used Infercnvpy[30], a Scanpy[65] plugin, to infer CNVs from scRNA-seq data in order to
771 identify tumor cells. Data were normalized and logarithmized (base *e*) in Scanpy. Window size
772 was set to 500 genes. Identified tumor cells matched and validated our annotation of tumor
773 cells based on gene expression. Cells from various non-malignant cell types were then used as
774 reference categories to set the background CNV profile.

775 ***Meta-module scoring***
776 The calculation was performed according to the algorithm described by Neftel *et al.*[5] The code
777 was implemented in Python and first validated on the dataset from Neftel *et al.* to ensure the
778 results matched the original publication. Every cell has four different scores, each representing
779 the substates (including the MES-state score).
780
781 ***Differential gene expression***
782 Data were normalized and logarithmized in Scanpy[65]. The Scanpy function
783 "rank_genes_group" was used to rank genes according to Z-score (Wilcoxon) and the
784 corresponding significance-level (p-value). Genes were plotted according to its scores (ranking
785 top 20 genes) and visualized in a volcano plot. Genes that are part of the MES-genes according
786 to Neftel *et al*. were encircled in red.

787 ***EEL-FISH probe design***
788 The RNA-binding encoding probes were designed to previously reported specifications[12] using
789 Oligopy (https://github.com/linnarsson-lab/oligopy). Gene identities were encoded in 16-bit
790 binary barcodes, with each barcode containing six positive bits to be read out in a single
791 fluorescence channel, thus allowing up to 448-plex gene detection per fluorescence channel
792 over 16 rounds of imaging. In total, we used three different encoding probe panels, each
793 designed to be read out in different fluorescence channels for orthogonal detection. Two of
794 these panels constituted the 888 genes used in further analysis; the third panel was used only
795 as a back-up for a subset of the 888 main genes.

796 Encoding probes (produced as Oligo Pools, Twist Bioscience) were amplified in-house. Probe
797 amplification was carried out separately for each of the three probe sets, following a previously
798 published protocol[66]. A modification was made to the original protocol in the reverse
799 transcription reaction: a 5′-amine-modified forward primer was used to improve encoding
800 probe anchoring during formaldehyde fixation in the EEL-FISH protocol. The RNA input
801 concentration for the reverse transcription step was limited to approximately 150 ng/µl.

802 Readout probes (IDT) contained 20-nucleotide-long sequences complementary to the detection
803 sequences on the encoding probes and a disulfide-conjugated fluorophores (Cy3, Atto 590 or
804 Alexa Fluor 647) on either 5'- or both 5'- and 3'-ends.

805 All probe and primer sequences are available in Supplementary Table 4.

806 ***EEL-FISH***
807 EEL-FISH was performed as previously described[12], with a digestion buffer adapted for
808 glioblastoma tissue. Namely, the digestion buffer contained 1% (wt/vol) sodium dodecyl
809 sulfate (SDS, Sigma-Aldrich), 20 mM tris-HCl pH 7.4 (Thermo Fisher Scientific), 100 U/ml
810 Superase RNase inhibitor (Thermo Fisher Scientific), and 0.8 U/ml proteinase K (NEB). The
811 samples incubated with the modified digestion buffer four times for five minutes at 30°C,
812 followed by four washes with pre-warmed 5% (wt/vol) SDS in 2× SSC (Sigma-Aldrich) for
813 five minutes each at 30°C. We noticed high variability in glioblastoma tissue sensitivity to the

digestion treatment and therefore we strongly recommend adjusting the proteinase K concentration and the number of digestion buffer washes for each sample individually.

Tissue sections adjacent to EEL-FISH section were used for H&E (Hematoxylin and Eosin stain kit; Vector laboratories; see https://protocols.io/view/hematoxylin-amp-eosin-staining-protocol-djrr4m56 for full protocol).

EEL-FISH image acquisition

EEL-FISH image acquisition was performed on a Nikon Ti2 epifluorescence microscope equipped with a Nikon CFI Plan Apo Lambda ×60 oil immersion objective with a numerical aperture (NA) of 1.4, CFI Plan Apo Lambda ×40 objective with NA 0.95, CFI Plan Apo Lambda ×10 with NA 0.45, Nikon motorized stage, Nikon Perfect Focus system, Sona 4.2B-11 back-illuminated sCMOS camera with a pixel size of 11 µm (Andor). We used Lumencor Spectra light engine and matching filter cubes from Chroma. Namely, fiducial europium beads were imaged using 360/28 bandpass filter (400 mW light source; 30% power), ET667/30m emission filter, and T647lpxr dichroic mirror; Cy3 channel was imaged using 534/20 bandpass filter (400 mW light source, 100% power), ET575/40m emission filter, and T550lpxr dichroic mirror; Atto 590 channel was imaged using 586/20 bandpass filter (400 mW light source, 100% power), 89403X excitation filter, 89403m multiband emission filter, and 89403bs dichroic mirror; Alexa Fluor 647 channel was imaged using 631/28 bandpass filter (500 mW light source, 100% power), ET667/30m emission filter, and T647lpxr dichroic mirror, with all exposure times set to 100 ms.

Histology image acquisition was performed at Karolinska Institutet's Biomedicum Imaging Core facility on a Zeiss Axio Scan.Z1 slide scanner.

Flow cytometry

Samples were minced with a scalpel into ~1-3 mm pieces and digested in RPMI-1640 medium (Cytiva) containing 0.25 mg/ml DNase I (Roche) and 0.25 mg/ml Collagenase (Sigma-Aldrich) at 37 °C for 25 min with stirring, strained through a 70-µm strainer and neutralized by adding RPMI-1640 with 10% heat inactivated FBS (HI FBS; Gibco).

Flow cytometry was performed as previously described[67]. Briefly, cells were stained for 20 min at RT with extracellular antibodies in a staining mix containing FACS buffer (1× dPBS (Sigma-Aldrich) with 2% HI FBS and 2 mM EDTA (Invitrogen)), 1:5 BD Horizon Brilliant Stain buffer (BD Biosciences), and 1:25 FcR blocking reagent (Miltenyi), followed by fixation using BD FixPerm buffer (BD Biosciences) for 30 min at RT, and staining with intracellular antibodies in BD Perm/Wash buffer (BD Biosciences) for 20 min at RT. Flow cytometry was performed on a FACSymphony A5 (BD Biosciences), fcs files generated using DIVA (BD Biosciences) and data analyzed in FlowJo v10.5.3 (BD Biosciences).

Glioblastoma organoid culture

Organoids were grown as described in Jacob *et al.*[68] from patient samples described above. Organoids were biobanked in liquid nitrogen at passage 0-1, revived and grown to passage 3-4. Organoids of homogenous size and shape were selected for experiment and grown in 4 ml medium per condition in 6-well plates with continuous shaking. For blood plasma condition, medium containing 10% human plasma (Merck) was prepared by decreasing the volume of DMEM/F12 and Neurobasal medium, while the concentrations of supplements were identical to the standard medium. For hypoxia condition, organoids were grown in moderate hypoxia (5% O_2, 5% CO_2) for the first 24 h and severe hypoxia (2% O_2, 5% CO_2) from timepoint 24 h to 72 h.

859 ***Xenium sample preparation***
860 Organoids were washed with 1× PBS (Thermo Fisher Scientific), fixed in 4% formaldehyde
861 (Thermo Fisher Scientific) in 1× PBS for 10 minutes and washed again with 1× PBS three
862 times. Before freezing, organoids were cryoprotected by allowing to sink in 15% and then 30%
863 sucrose (Sigma Aldrich) solutions in 1× PBS. Xenium (v1 platform, Human Brain panel with
864 custom add-on genes; 10x Genomics; Supplementary Table 4) experiments were performed by
865 the In Situ Sequencing Infrastructure Unit, SciLifeLab Stockholm.

866 ***Image processing***
867 We used pysmFISH (https://github.com/linnarsson-lab/pysmFISH_auto) to automatically
868 detect and decode the EEL-FISH signal. Briefly, after parsing, images were filtered, and large
869 objects with a size over the 95th quantile were removed. Then, spots were counted and
870 registered between hybridizations using europium fiducial beads. The barcodes were then
871 identified using a nearest-neighbor approach. To map the EEL-FISH signal (×60 objective) to
872 nuclei images (×40 objective), we first registered the europium beads imaged with both
873 objectives by using a point set alignment algorithm based on a nearest-neighbor search, and
874 the resulting transformation (scaling, rotation and shift) was applied to the EEL-FISH signal.
875 Nuclei were segmented using Cellpose[69]. To process the large amount of data generated by
876 each EEL-FISH experiment, the analysis is parallelized using Dask[70]. EEL-FISH data were
877 aligned to histology images based on nuclei masks using SimpleElastix (affine transformation
878 with 15 resolutions and 2500 iterations; https://github.com/SuperElastix/SimpleElastix).

879 ***M-state Graph Attention Network***
880 Transcriptional States, m-states, were inferred using a cell-free segmentation approach using a
881 graph attention neural network (GAT) as previously proposed by Partel and Whalby[71]. Only
882 the 888 RNA species common to all EEL-FISH experiments were used for analysis. *GFAP* and
883 *MOG* molecules were removed due to their extremely high counts. First, molecules were
884 connected into an undirected graph if the distance between two molecules was below the 95th
885 quantile at which all molecules were connected to at least 3 neighboring molecules (~5-10 µm).
886 Nodes in the graph represent RNA molecules and every node has a feature vector which is a
887 one hot encoding the identity of the RNA transcript, edges in the graph connect neighboring
888 molecules. We generated a graph for each EEL-FISH sample and pruned all graphs by
889 removing molecules connected to less than 5 neighbors. The GAT was designed using PyTorch
890 (https://pytorch.org) and Deep Graph Library (https://www.dgl.ai/) with the following
891 architecture: 2-hop neighbor aggregation using GAT2vCONV[72,73] module from DGL and a
892 final linear layer; and the following hyperparameters: a random sampling strategy with 20 and
893 10 neighbors for 1st and 2nd hop, respectively, 64 units for each hidden layer and 48 units for
894 generated lower dimensional embedding. The GAT was trained using Adam as optimizer[74]
895 with a learning rate of 0.0001 and mini-batch sampling of 512 nodes per iteration. Model
896 parameters are learned using an unsupervised method under the premise that neighboring RNA
897 molecules in the should have similar embeddings, whilst distant molecules should have
898 dissimilar embeddings. During training, embeddings are generated for *positive* nodes, true
899 neighbors, and *negative* nodes, randomly sampled nodes, from each central node and the
900 model's objective function consists of the binary cross-entropy between *positive* and *negative*
901 embedding for each sampled node.

902 We trained our generalized GBM-GAT for 10 epochs on 2-hop subgraphs generated from
903 500,000 random nodes, from 30% of our EEL-FISH sections, constituting a graph for training
904 with a total of 33.6 million nodes and 359.7 million edges. The generated embedding for all
905 central nodes was clustered into 80 different m-states using sklearn function *MiniBatchKMeans*
906 and a sklearn *SGDClassifier* was trained using the generated embedding to predict cluster id

907 from GAT embedding vectors. Next, we applied our generalized GBM-GAT to each individual
908 EEL-FISH section graph and classified each RNA into the 80 spatial domains using the trained
909 classifier. RNA molecules with a prediction probability below 50% to a spatial domain were
910 discarded. Finally, we reduced m-states to 42 after merging m-states with gene expression
911 correlation over 85%.

912 ***M-cell segmentation***
913 To facilitate further analysis, m-states were segmented using a combination of DBscan and
914 QTclustering. First, sklearn function *DBscan* was applied to each individual m-state using 20
915 and 10 for the parameters_*eps* and *min_samples*, respectively. Next, we re-segmented DBscan
916 outputs, if they had a maximum distance over 50 µm, using QTclustering algorithm with
917 parameters *max_radius* and *min_cluster_size*, 20 and 10, respectively. We removed m-cells
918 with less than 10 molecules. Finally, m-cells were kept if the distance to closest cell nuclei was
919 below 50 µm.

920 ***M-state annotation***
921 Annotation of m-states was done by combining Tangram[40] predictions and gene enrichment
922 scores. First, we used Tangram to map all m-states gene expression from all samples to
923 GBmap[41] averaged expression of tumor states, immune cells, and oligodendrocytes. Gene
924 expression from each m-state was normalized to 10,000 molecules per m-cell and Tangram
925 was run using the following parameters: *mode*='clusters', *num_epochs*=1000,
926 *density_prior*='uniform' and *lambda_g2*=1. The probability of each m-state for each reference
927 cluster was averaged for all samples. The same procedure was repeated to map the m-states to
928 human developmental scRNA-seq data[42].

929 Gene enrichment was calculated for every m-state and sample using Cytograph's enrichment
930 score function *Enrichment*.

931 Multi-region sample SL040 was used to re-classify AC-like m-cells as either non-tumor
932 astrocytes (periphery samples) or AC-like tumor astrocytes (high-fluorescence zone). A linear
933 classifier (CellTypist[75]) was trained on samples from the periphery or high-fluorescence zone
934 from sample SL040. The classifier was applied to the remaining EEL-FISH samples to
935 reclassify non-tumor astrocytes m-states accordingly.

936 ***scVI integration of organoid data***
937 We utilized scVI[49] to model gene expression profiles from xenium organoid data. We trained
938 two models, with and without patient-line correction, to account and assess the biological and
939 technical variability that arise from using 4 different patient GBM organoid lines, 3 different
940 conditions (hypoxia, blood plasma, and both), and 4 different time points (0, 24, 48 and 144
941 hours). Leiden clustering was used to identify common molecular profiles across all conditions
942 and patients using the batch-corrected latent space from scVI.

943 ***Generalized linear model of Wound Response activation-deactivation in organoids.***
944 We implemented a generalized linear model (GLM) in PyMC[76] to model the expression of each
945 gene as a Poisson-distributed variable, using Markov chain Monte Carlo (MCMC) to infer the
946 posterior distributions for the effect sizes of hypoxia, plasma, their interaction, and distance to
947 core (eq1. and eq. 2); where β, d, h, p, and k are the intercept, effect size of the distance to core,
948 hypoxia, blood plasma, and interaction effect for hypoxia and plasma, respectively. We used
949 non informative normal priors with a zero-centered mean and standard deviation of 5. Time (t)
950 was indicated as either 0 (for time 0 h and 144 h) or 1 for time 24 h or 48 h under hypoxia,

plasma or both. Distance to core (D) was normalized between 0 and 1. Posterior distributions were inferred using PyMC NUTS sampler.

$$\text{Equation 1: } Expression \sim Poisson\left(e^{\lambda}\right)$$

$$\text{Equation 2: } \lambda = e^{-d \cdot D}\left(\beta + t(hH + pP + kK)\right)$$

Wound Response pseudotime

We used scFates[50] to infer a pseudotime for the activation of wound response on the EEL-FISH data. We used the m-states identified as WR from all EEL-FISH samples, filtered cells with less than 5 molecules, normalized, log-transformed, scaled, and obtained the principal components using only highly variable features. The scFates function sc.tl.curve was used to build a graph using the following hyperparameters (*ndims_rep=2, epg_mu=.5*). The root was defined as the closest to highest *AQP4* and lowest *VEGFA* expression. Next, cells were projected into the pseudotime, and genes were clustered into different modules/trends.

Neighborhood enrichment and graphs

Squidpy[77] functions were used to calculate the enrichment scores for all possible m-state pairs. First, *spatial_neighbors* function was used to build a neighborhood graph connecting each m-cell to the 10 nearest m-cells below 100 µm distance and used Delaunay triangulation. Then, we used *neighborhood_enrichment* to obtain the spatial proximity scores for each pair based on permutation test.

We calculated a spatial similarity dendrogram based on each tumor sample enrichment score. First, enrichment score matrices were vectorized and rearranged so that each vector entry corresponded to the enrichment score for the same m-state pair in each sample. Next, each vector was scaled and pairwise cosine distances calculated to build a dendrogram using *ward* method.

The TAM and GW neighborhood graphs were built using the previously calculated enrichment scores. To build the graph, we used each m-state in each pair as nodes and connected nodes whose enrichment score was above 8.5 to enrich for highly enriched interacting m-states. We used NetworkX (https://networkx.org) *spring_layout* to facilitate graph visualization.

Neighborhood in situ enrichment

Neighborhood *in situ* interaction score was built based on the neighborhood enrichment scores. First, m-cells were binned in a hexagonal grid. Next, a vector field was computed by calculating the average enrichment interaction vector between the central hexagon and its neighboring hexagons. Each enrichment interaction vector was calculated as the original distance vector between each hexagon pair multiplied by the total number of m-state pairs found across hexagons multiplied by their enrichment score. The final enrichment *in situ* score was obtained by assigning m-cells to the value of their closest vector module.

Single m-cell analysis

To analyze tumor m-states, m-cells were pooled from all samples. Cells with a total number of molecules below and above the 5th and 95th quantiles were removed. Top 500 highly variable genes were selected for downstream processing. We normalized the total number of molecules to l2-norm, performed log transformation and *minmax* scaling per each individual sample to remove batch effects. PCA was run and sample specific batch effects were corrected using Harmony. UMAP dimensionality reduction was computed. Gliosarcoma and myeloid cell

pools did reveal significant batch effects; in these cases, total counts were normalized, and log-transformed, sample min-max scaling and Harmony correction were not required. Clustering was not necessary as m-states were used for further analysis.

Data visualization

We used FISHscale (https://github.com/linnarsson-lab/FISHscale) for the spatial visualization of RNA molecules and FISHspace (https://github.com/linnarsson-lab/FISHspace) for the visualization of m-cells as polygons. FISHspace software was developed based on the Python package stlearn[78], with some added functionalities for visualization and pseudotime analysis.

DATA AVAILABILITY

EEL-FISH molecule coordinates, accompanying H&E images and Xenium data are available at BioImage Archive. Raw EEL-FISH image data will be shared by the lead contact upon request. Corresponding gene expression data have been deposited on google storage and can be accessed at https://github.com/linnarsson-lab/glioblastoma_wound_response. The m-cell segmented data is available in AnnData format compatible with scanpy, squidpy, and FISHspace. The EEL-FISH RNA coordinates are available as parquet files compatible with FISHscale. Raw scRNA-seq data are available at European Genome-phenome Archive under Accession number TBA. The dataset can also be browsed and downloaded at CELLxGENE (https://cellxgene.cziscience.com/collections/113a558a-e96e-4643-81db-140e95c58578).

CODE AVAILABILITY

All original code has been deposited at https://github.com/linnarsson-lab/FISHscale for the analysis and visualization of RNA molecules and https://github.com/linnarsson-lab/FISHspace for m-cell analysis and visualization. Single-cell RNA sequencing data were analyzed using Cytograph-Shoji (https://github.com/linnarsson-lab/cytograph-shoji). Code for general data visualization can be found at https://github.com/linnarsson-lab/glioblastoma_wound_response.

ACKNOWLEDGEMENTS

We thank Anna Johnsson, Karolinska Institutet, for grant management and all members of the Linnarsson lab for helpful discussions. We thank the Biomedicum Imaging Core Facility, Karolinska Institutet, and the In Situ Sequencing Infrastructure Unit, SciLifeLab Stockholm, for their services. In addition to author O.P., we would like to thank neurosurgeons Margret Jensdottir and Jiri Bartek and all other neurosurgeons and nurses at the Department of Neurosurgery at Karolinska University Hospital for tissue collection, and patients for donating tissue. This work was supported by Region Stockholm (support to J.K.J.) and the Erling-Persson Family Foundation (Atlas of childhood disease), Hjärnfonden (FO2023-0309), the Swedish Research Council (2022-01248), and the Torsten Söderberg Foundation grants to S.L.

AUTHOR CONTRIBUTIONS

O.P., J.K.J., and S.L. conceived and designed the multi-region scRNA-seq study. J.K.J. and L.H. performed scRNA-seq experiments. J.K.J., K.S. and S.L performed scRNA-seq data analysis. S.L., A.M.A., and J.J. conceived the spatial transcriptomics study. J.J. and A.M.A. performed EEL-FISH experiments, I.K. performed other stainings. R.K. derived organoids from primary tumor tissue. R.K., M.C.M.F. and I.K. performed organoid experiments. L.E.B., A.M.A. and J.J. optimized the EEL-FISH protocol. A.M.A. performed data analysis. S.C. developed and performed image analysis. E.K. and J.B.M. performed flow cytometry

experiments and analysis. O.P. and J.K.J. provided tumor specimens and clinical annotation. A.S. performed pathology analysis. A.M.A., J.J., J.K.J. and S.L., interpreted the results and wrote the manuscript. All authors provided critical feedback and helped shape the project, analysis and the manuscript.

COMPETING INTEREST DECLARATION

S.L. is a paid scientific advisor to Moleculent and a shareholder in EEL Transcriptomics AB, which owns the intellectual property to the EEL method ("Spatial RNA localization method", provisional US patent application 63/139,701). All other authors declare that they have no competing interests.

ADDITIONAL INFORMATION

Supplementary Information is available for this paper. Correspondence and requests for materials should be addressed to the lead contact, Sten Linnarsson (sten.linnarsson@ki.se).

EXTENDED DATA

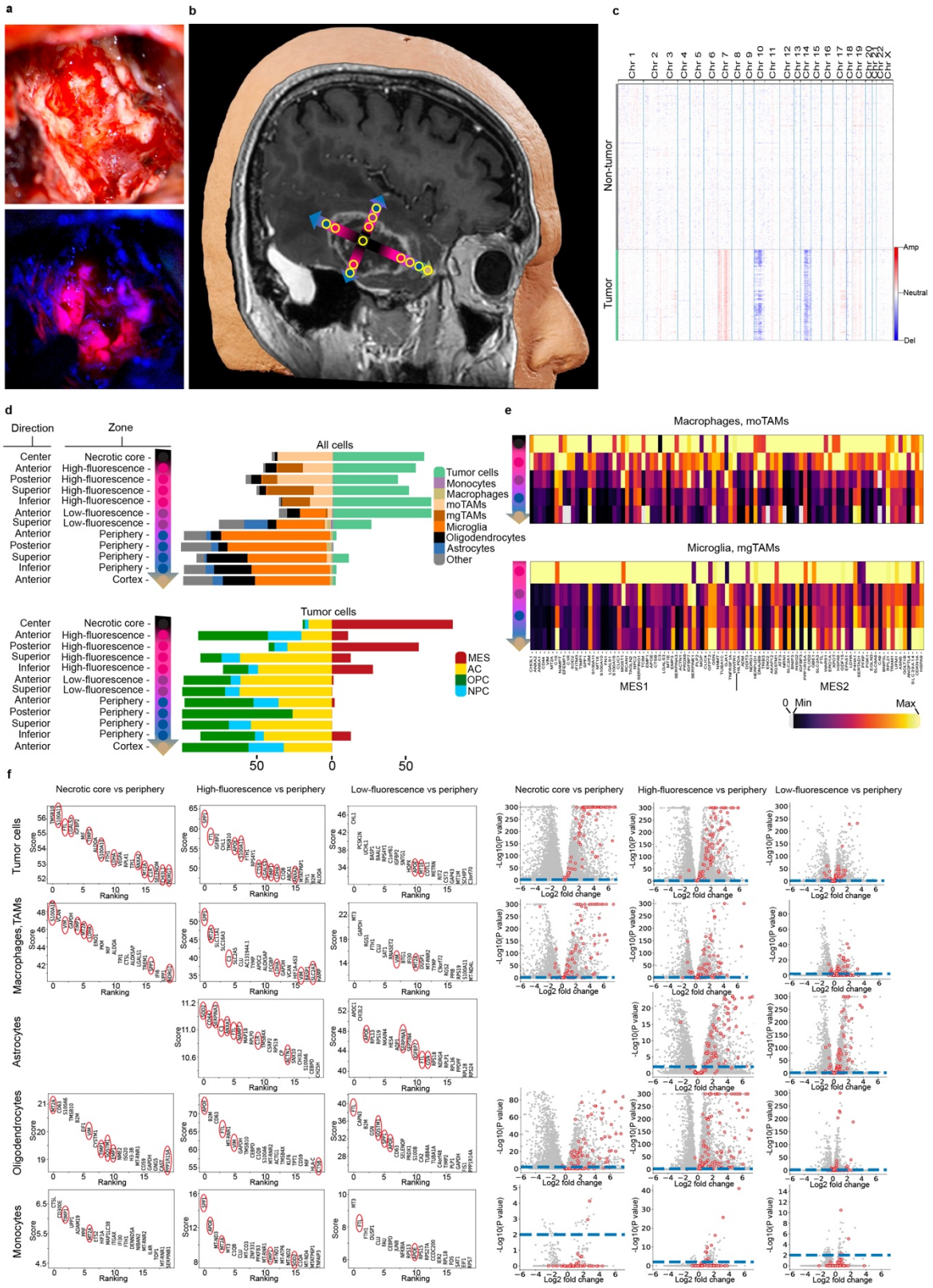

Extended Data Figure 1. **scRNA-seq analysis of multi-region sample SL040. a**, Images of GBM surgery. Top: Surgical area visualized in white light. Bottom: Same area with fluorescence microscopy in blue light visualizing areas with high-fluorescence (red), low-fluorescence (pink/purple) and no fluorescence (blue and black). **b**, 3D reconstruction of MRI in Brainlab Elements, sagittal plane of

1055 SL040. Arrows are colored according to fluorescence and show directions of sampling for scRNA-seq.
1056 Yellow circles schematically visualize sampling locations. **c**, Heatmap of the inferred CNV profiles in
1057 SL040 across chromosomes (columns) and single cells (rows) from scRNA-seq data. Annotation of
1058 cell types (tumor, non-tumor) based on gene expression profiles and clustering on the tSNE. **d**, Top:
1059 Bar charts of scRNA-seq cell type proportions in all 12 sampling locations annotated by direction and
1060 zone. Bottom: Bar charts of tumor cell state fractions in sampling locations. **e**, MES-like gene
1061 expression in the macrophage lineage (macrophages, moTAM) and microglia lineage (microglia,
1062 mgTAM) across zones (no microglia lineage cells in necrotic core). The colormap shows linear gene
1063 expression from the minimum to the maximum value per gene, with zeros shown in gray. **f**, Differential
1064 gene expression by zone (columns) and cell type (rows). No analysis of astrocytes in the necrotic core
1065 due to small sample size (number of cells = 2). Left: ranking of the top 20 differentially expressed genes
1066 between tumor zones by z-score. MES-like genes are encircled in red. Right: volcano-plots of
1067 differentially expressed genes between tumor zones, MES-genes are encircled in red (blue line, $q <$
1068 10^{-2}).

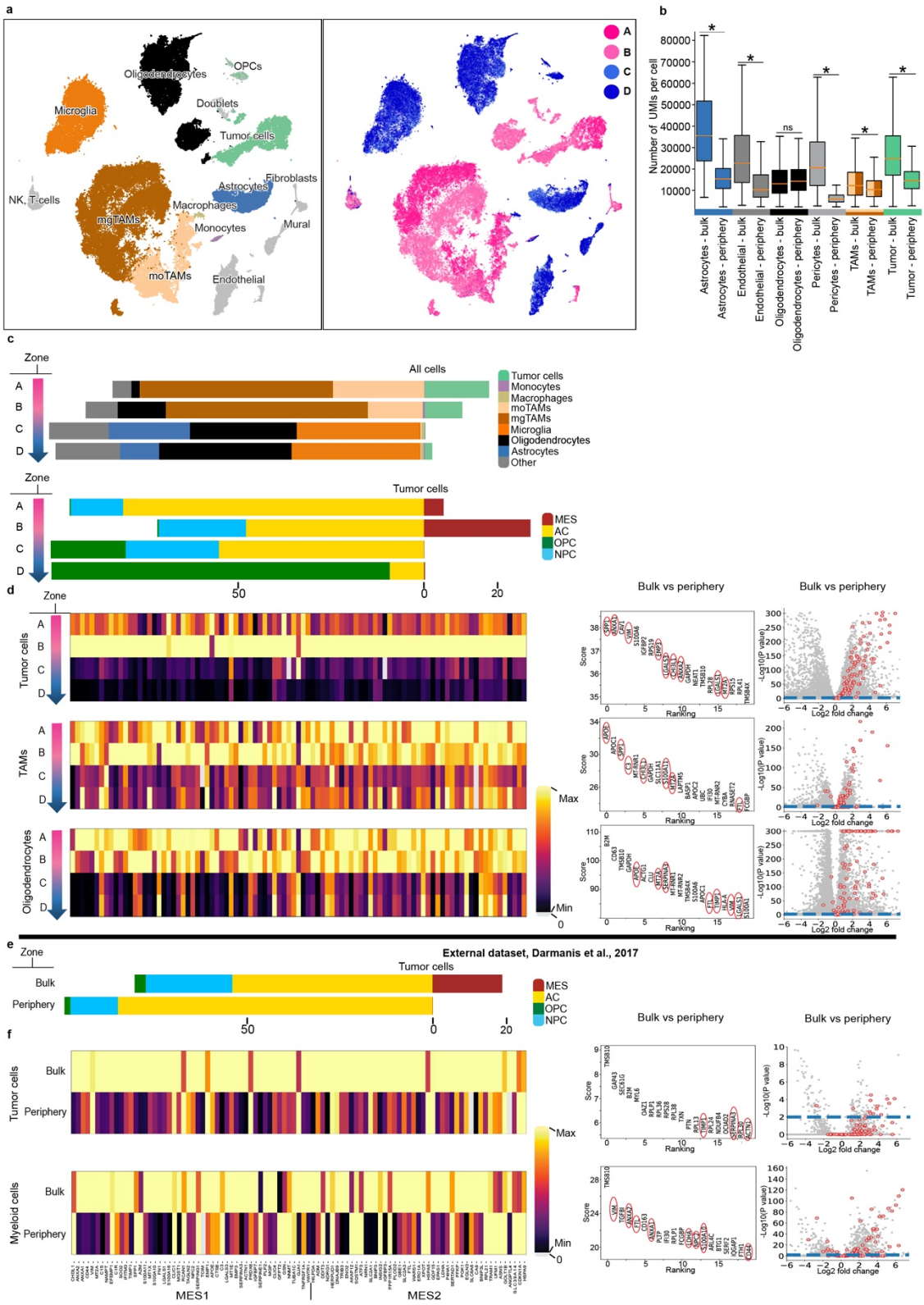

Extended Data Figure 2. scRNA-seq analysis of multi-region sample SL057 and an external dataset. a, t-SNE representation of scRNA-seq data from sample SL057, spanning from tumor bulk (A, B) to periphery (C, D). **b**, Distribution of total UMIs per cell in various cell types by sampling location (bulk/periphery) in SL040 and SL057. Boxes are centered on the median and represents the first to third quartiles. Whiskers extend 1.5 interquartile range above and below the boxes. Asterisks indicate significant differences (Bonferroni-adjusted Mann-Whitney, one-sided ("greater") and $p < 1e10^{-18}$) for

1076 all cell types except oligodendrocytes ($p > 0.05$). **c**, SL057. Top: bar charts of scRNA-seq cell type
1077 proportions across all sampling locations. Bottom: bar charts of tumor cell state fraction across all
1078 sampling locations. **d**, Left: MES-like gene expression across cell types and zones in SL057. The
1079 colormap shows linear gene expression from the minimum to the maximum value per gene, with zeros
1080 shown in gray. Right: Differential gene expression by cell type (rows) and zone (columns). First column
1081 from left: ranking of the top 20 differentially expressed genes by z-score. MES-genes are encircled in
1082 red. Second column from left: Volcano-plots, MES-genes are encircled in red (blue line, $q < 10^{-2}$). **e**,
1083 **f**, External multi-region sample dataset from four patients[27]. **e**, Bar charts of tumor cell state fractions
1084 in sampling locations (bulk and periphery). **f**, Left: MES-like gene expression signature, Right:
1085 differential gene expression across cell types and zones.

1086

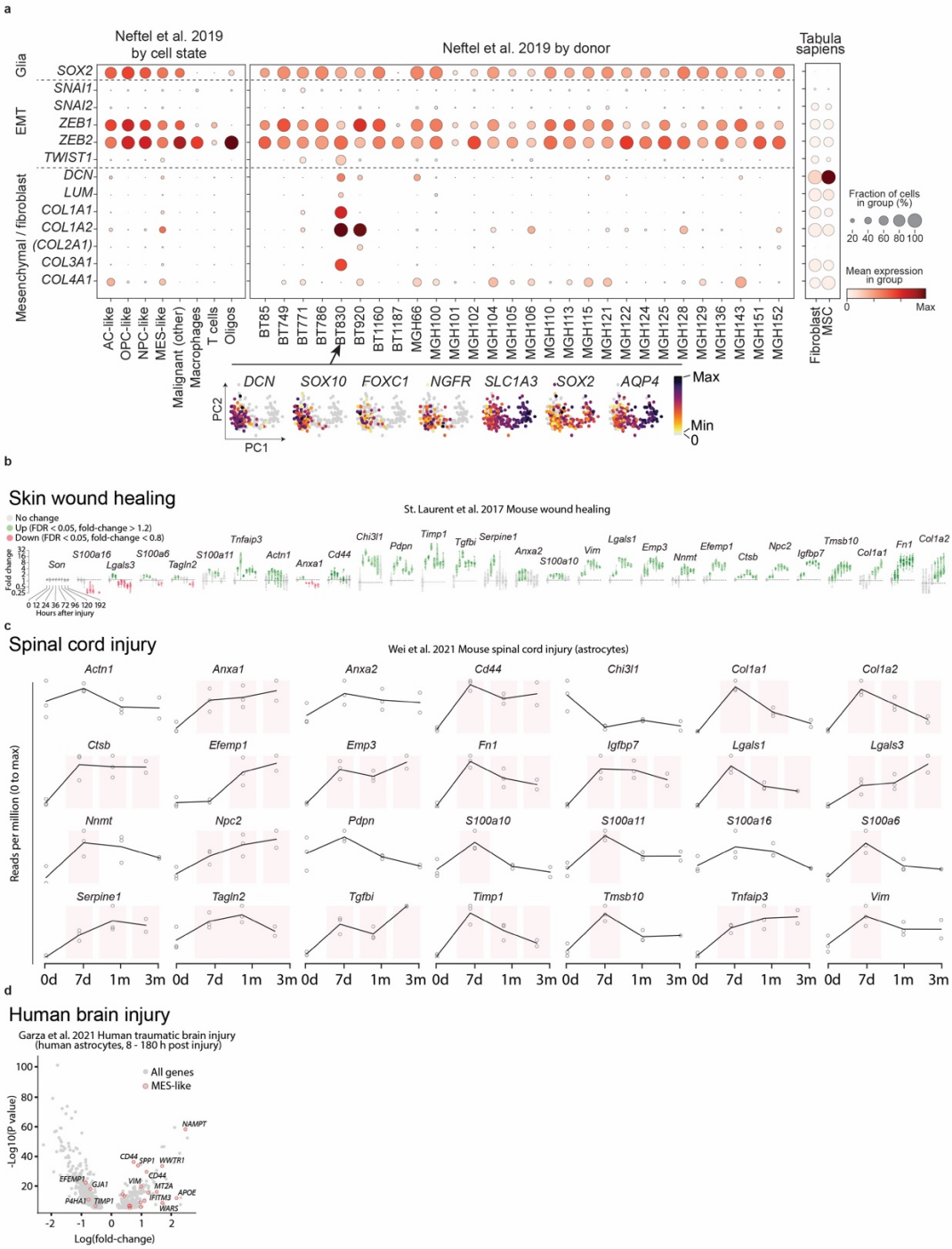

Extended Data Figure 3. Mesenchymal gene expression in MES-like cells and wound healing. a, Expression of mesenchymal marker genes in published datasets, Neftel *et al.*[5] and Tabula sapiens[48]. Mean expression is not necessarily comparable between datasets. Parentheses around *COL2A1* indicate that this gene is expected to be absent in mesenchymal cells. Arrow: putative gliosarcoma tumor. EMT, epithelial to mesenchymal transition. MSC, mesenchymal stem cell. At bottom, PCA projections of the cells from sample BT830, showing the expression of selected genes. Zeros are plotted in grey. **b**, Regulation of MES-core[37] genes during mouse skin wound healing[36]. Each plot shows the time-resolved expression of a MES-core gene (*SON* is shown as an example of an unregulated non-MES gene). Green, significantly up-regulated (FDR < 0.05, fold-change > 1.2); red, significantly down-regulated (FDR < 0.05, fold-change < 0.8). **c**, Regulation of MES-core genes in mouse spinal cord injury[38]. Red shading indicates significant up-regulation (FDR < 0.05). **d**, Regulation of MES-like[5] genes in human traumatic brain injury[39]. Red shows significantly regulated MES-like genes (FDR < 0.05; 18 up, 4 down).

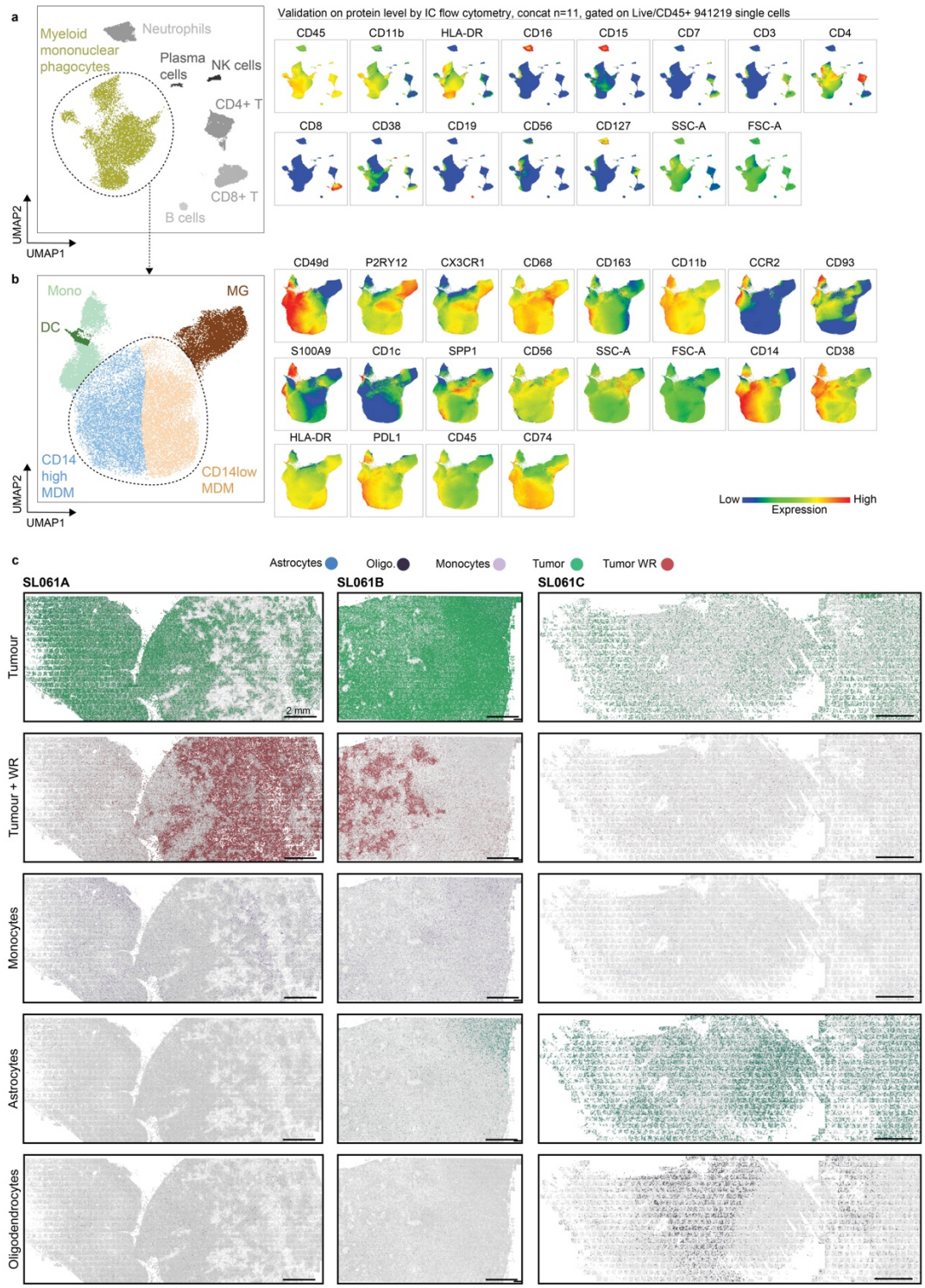

Extended Data Figure 4. Flow cytometry validation of immune cell populations and non-malignant versus non-malignant cell state classification in EEL-FISH. a, Left: UMAP representation of flow cytometry data from concatenated live immune cells ($CD45^{+}$) from 11 GBM samples not included in EEL-FISH cohort with gated myeloid mononuclear phagocytes. Right: corresponding cell identity marker expression. **b**, Left: UMAP representation of myeloid mononuclear phagocytes from A, showing monocytes (Mono), dendritic cells (DC), microglia (MG) and $CD14^{high}$ (blue) and $CD14^{low}$ (orange) monocyte-derived macrophages (MDM). Right: corresponding cell identity marker expression. **c**, Spatial distribution of malignant cells (WR and non-WR), astrocytes, oligodendrocytes and monocytes in a sample with multi-regional representation, SL061, from high-WR (left) to a low-WR (right) region.

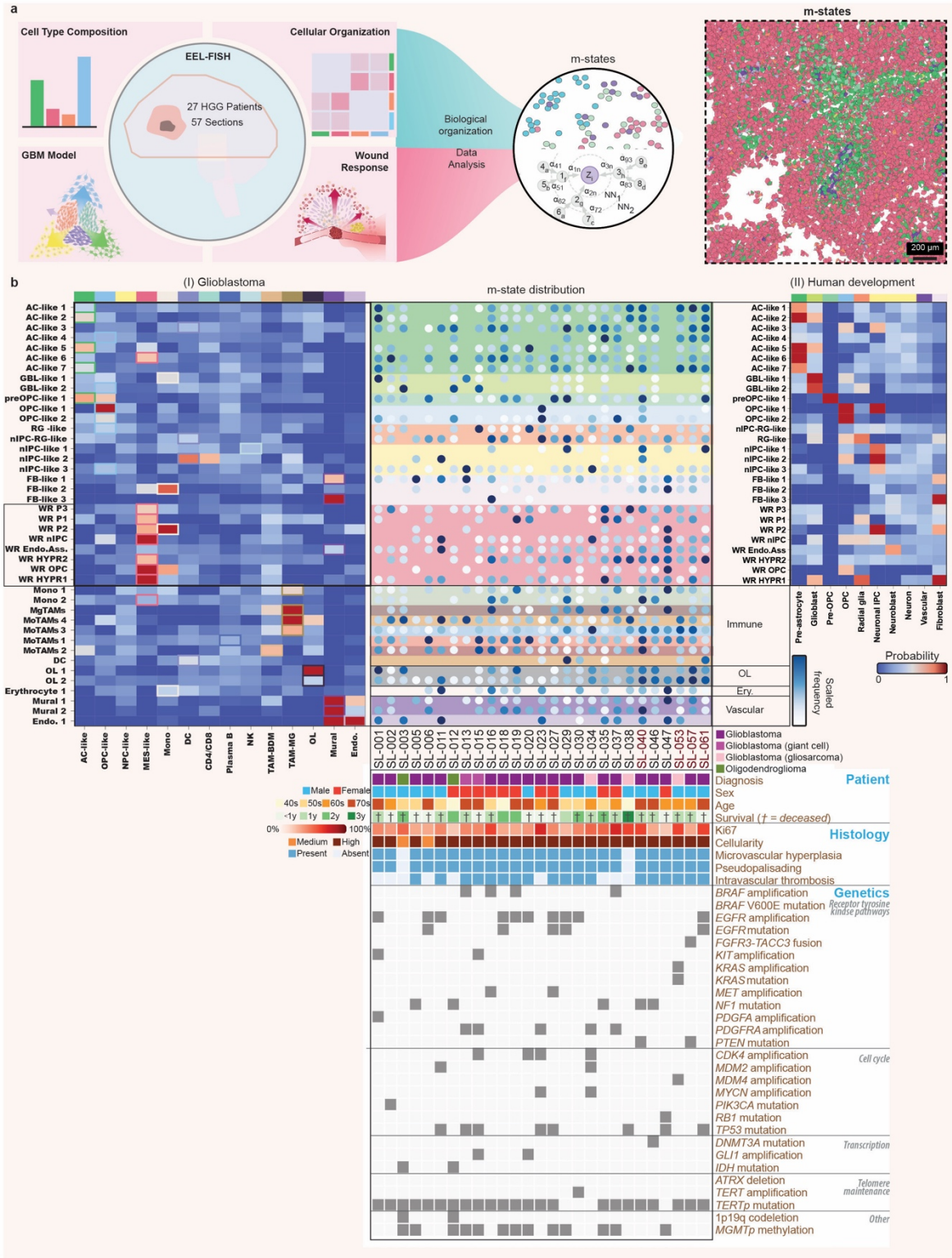

Extended Data Figure 5. Tangram mapping of m-states, m-state distribution across samples and pathology report summary. a, EEL-FISH analysis pipeline schematic for defining common m-states. **b**, Tangram mapping of m-states to scRNA-seq GBM reference[41] (left-most panel). Tangram mapping of m-states to a scRNA-seq human fetal development reference[42] (right-most panel). Dot plot of m-state distribution in samples from every patient (middle panel). Pathology report summary, patient information and tumor mutational profiles (bottom-panel). Names of multi-region samples are highlighted in dark red.

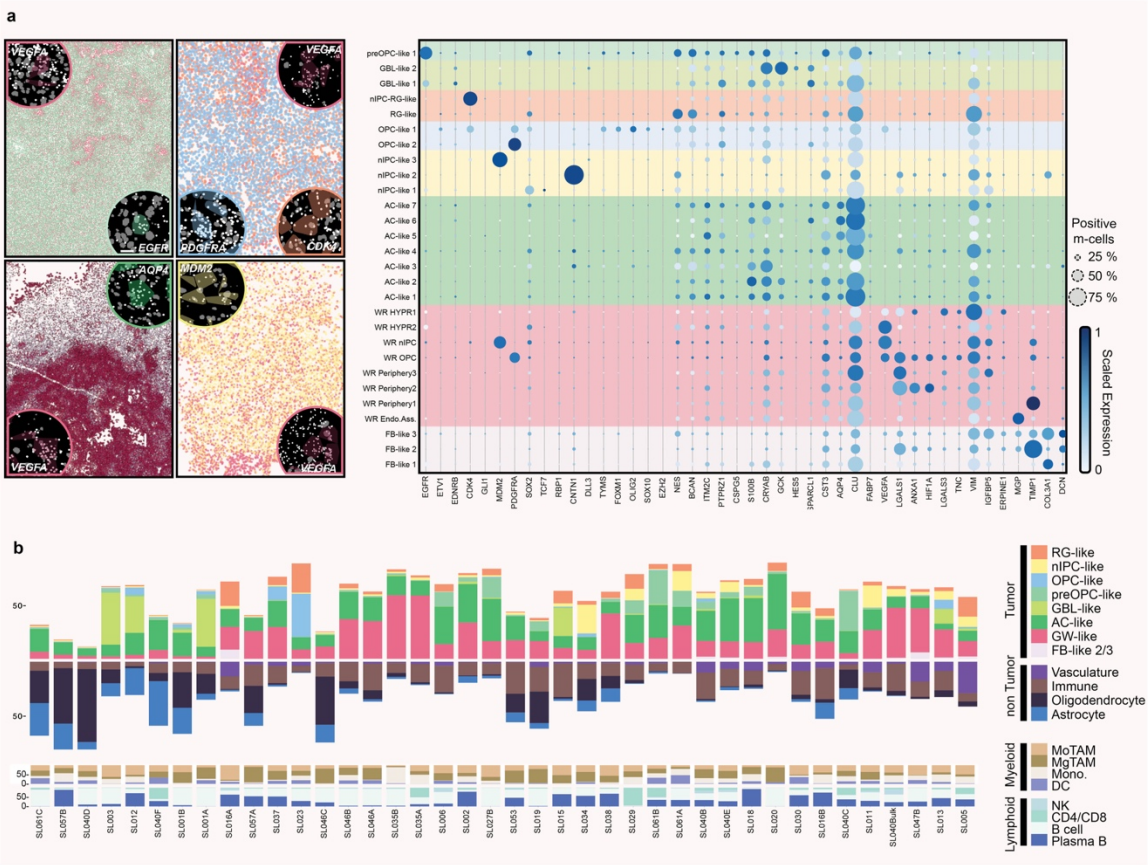

Extended Data Figure 6. Molecular characterization of GBM m-states using EEL-FISH. a, Left: WR marker VEGFA expression in samples with different predominant glia-like m-states (top left quadrant – sample SL061B, top right – SL023, bottom left – SL035B, bottom right – SL034). Colored polygons represent m-cells, gray polygons represent detected cell nuclei. M-state colors correspond to the right panel. Right: Dot plot showing the scaled marker gene expression for each tumor cell m-state. Dot size indicates the percentage of m-cells expressing each gene. **b**, Top: tumor and non-tumor m-state proportions across samples. Bottom: myeloid and lymphoid compartment composition across samples as represented by Tangram probabilities (percentage) for each scRNA-seq reference myeloid and lymphoid cell type as the sum of Tangram probabilities for all sample m-states.

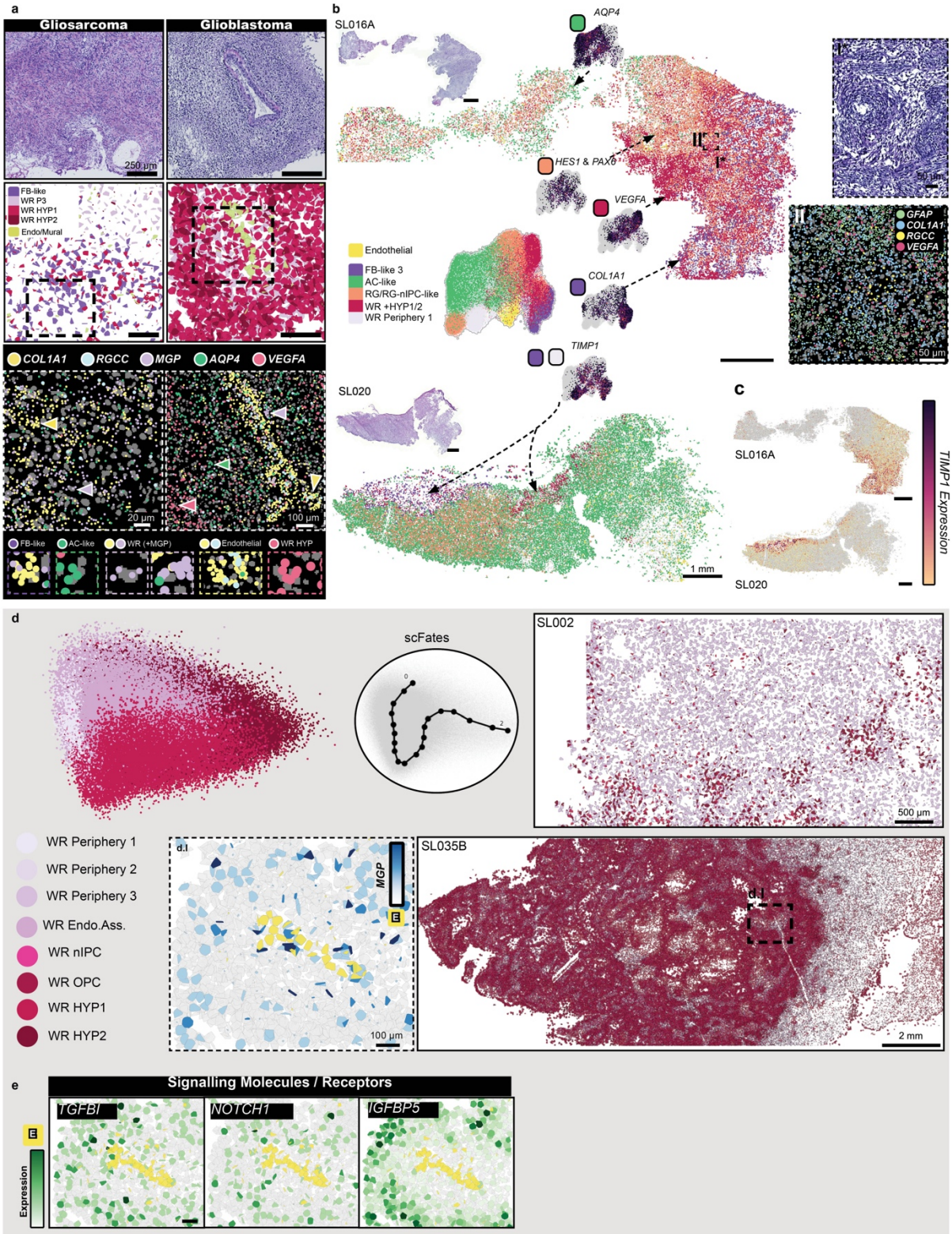

Extended Data Figure 7. Spatial and molecular characterization of fibroblast-like molecular states and generalized wound response in GBM. a, H&E staining, MES-like m-states, and marker gene expression in gliosarcoma (sample SL020) and glioblastoma (sample SL035B). **b**, Spatial distribution of FB-like and WR m-states in gliosarcoma. UMAP representation of endothelial, FB-like, WR and non-WR m-states in gliosarcoma. **c**, *TIMP1* expression in FB-like areas in gliosarcoma. **d**, Top left: Inferred pseudotime trajectory of WR states across all GBM samples. Spatial distribution of WR states in samples SL002 and SL035B. d.I: *MGP* expression in WR m-cells in a perivascular niche in sample SL035B. **e**, Expression of *TGFBI*, *NOTCH1* and *IGFBP5* in WR m-cells in a perivascular niche in sample SL035B (same area as d.I).

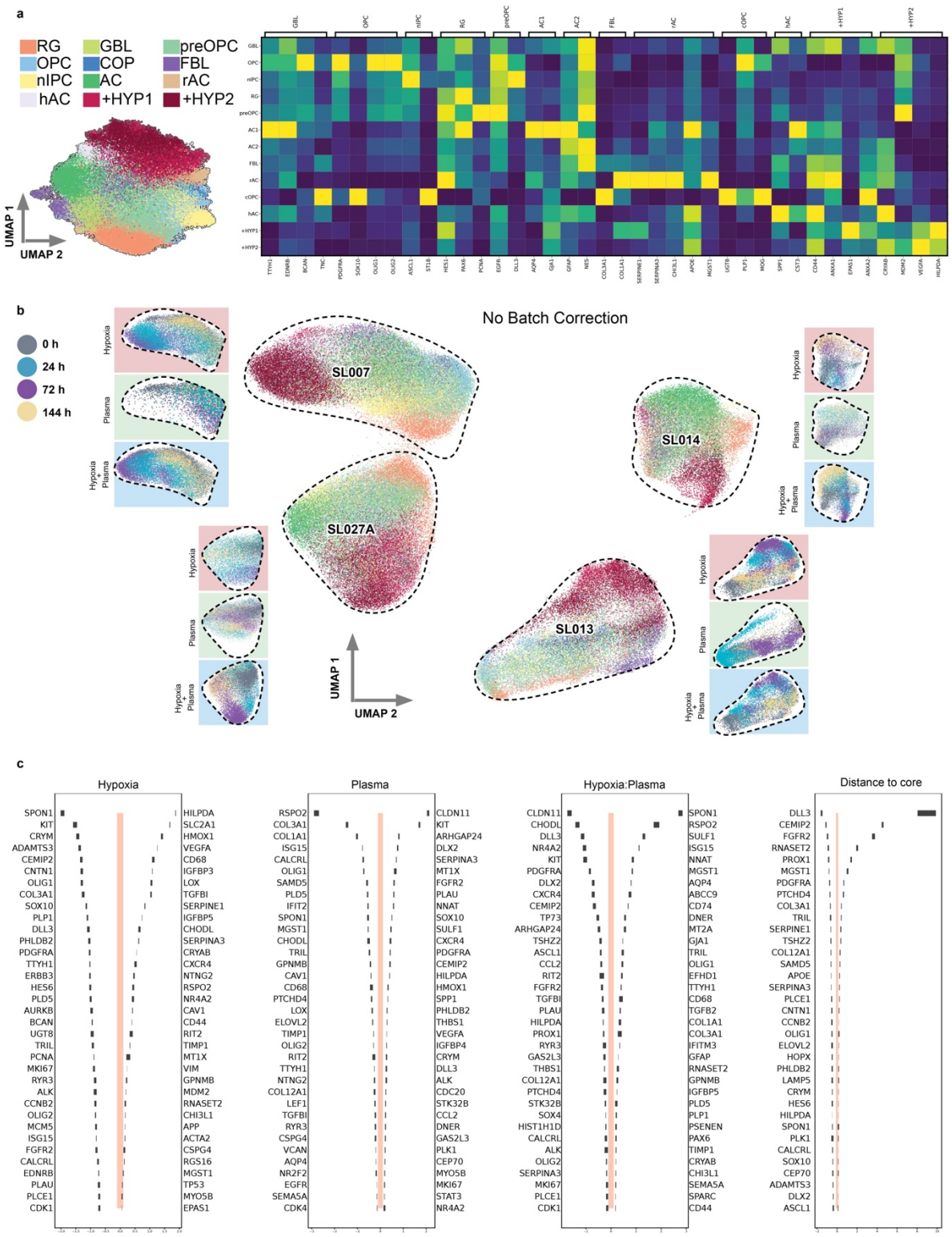

Extended Data Figure 8. Time-resolved changes in glioblastoma organoid molecular states under hypoxia, blood plasma or both. a, Left: UMAP representation of Xenium GBO data, batch corrected by patient. Right: heatmap of marker genes for each m-state. **b**, UMAP representation of non-batch corrected Xenium data across different culturing conditions and time points. **c**, Posterior distribution (quantile 5% and 95%) for the effect size of each gene under hypoxia, blood plasma, both and by distance to organoid core.

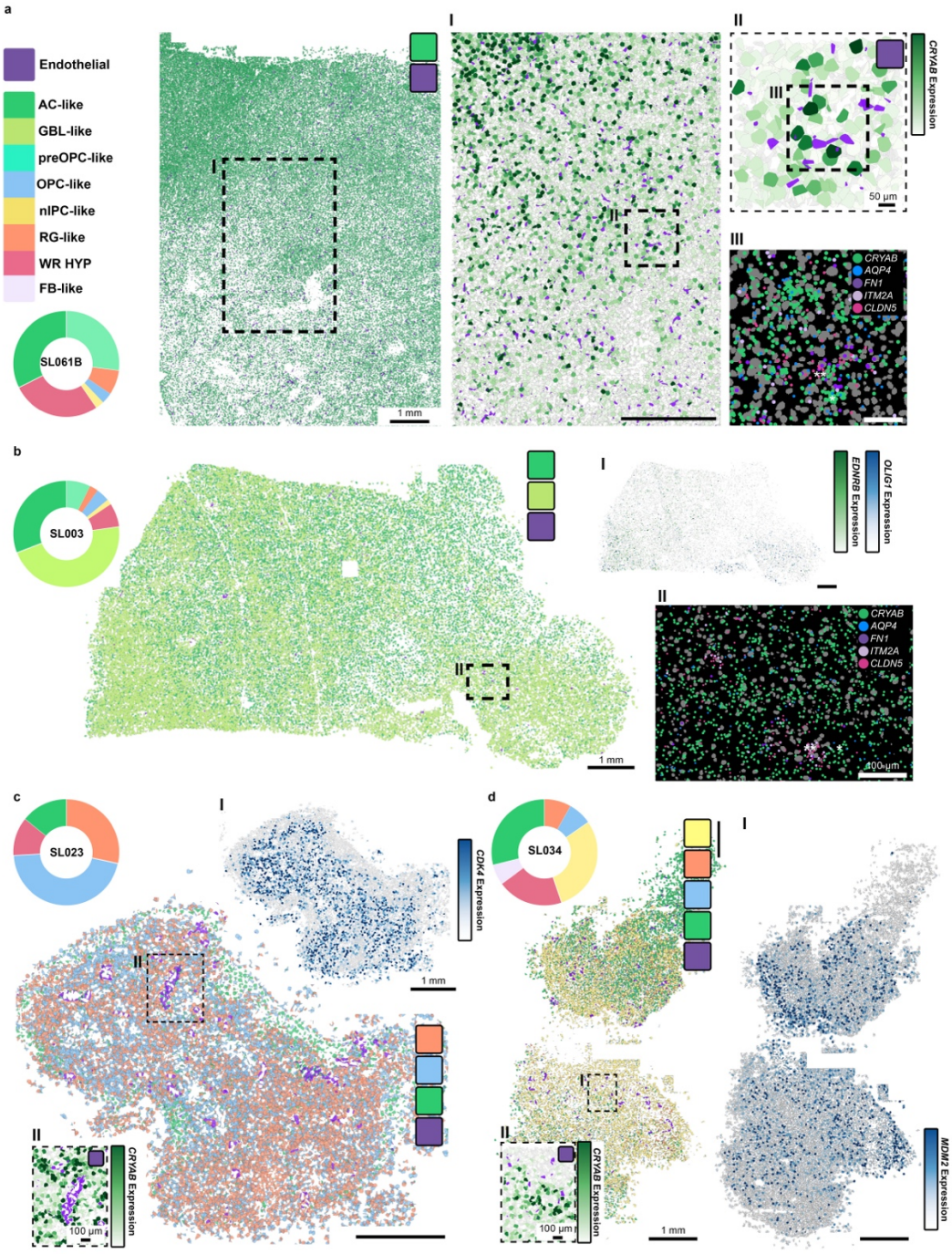

Extended Data Figure 9. AC-like and endothelial m-cell co-localization in GBM and oligodendroglioma. a, Spatial distribution of AC-like and endothelial m-states in sample SL035B; pie chart shows m-state proportions. I: Co-localization of *CRYAB* expression and endothelial m-cells. II: Close-up view of region I. III: Co-expression of AC-like markers *CRYAB* and *AQP4* (*) near endothelial cell marker genes *FN1*, *CLDN5* and *ITM2A* (**). Gray polygons represent m-cells with zero expression. **b**, Spatial distribution of AC-like, GBL-like and endothelial m-cells in oligodendroglioma sample SL003; pie chart shows m-state proportions. I: Expression of *OLIG1* and *EDNRB* in sample SL035B. Gray polygons represent m-cells with zero expression. II: Co-expression of AC-like markers *CRYAB* and *AQP4* (*) near endothelial cell marker genes *FN1*, *CLDN5* and *ITM2A* (**). **c**, Spatial distribution of OPC-, RG-, AC-like and endothelial m-cells in sample SL023 with corresponding *CDK4* expression. Gray polygons represent m-cells with zero expression. I: *CRYAB* expression surrounding endothelial m-cells. **d**, Spatial distribution of nIPC-, RG-, OPC-, AC-like and endothelial m-cells in sample SL034 with corresponding *MDM2* expression; pie chart shows m-state proportions. Gray polygons represent m-cells with zero expression. II: *CRYAB* expression surrounding endothelial m-cells.

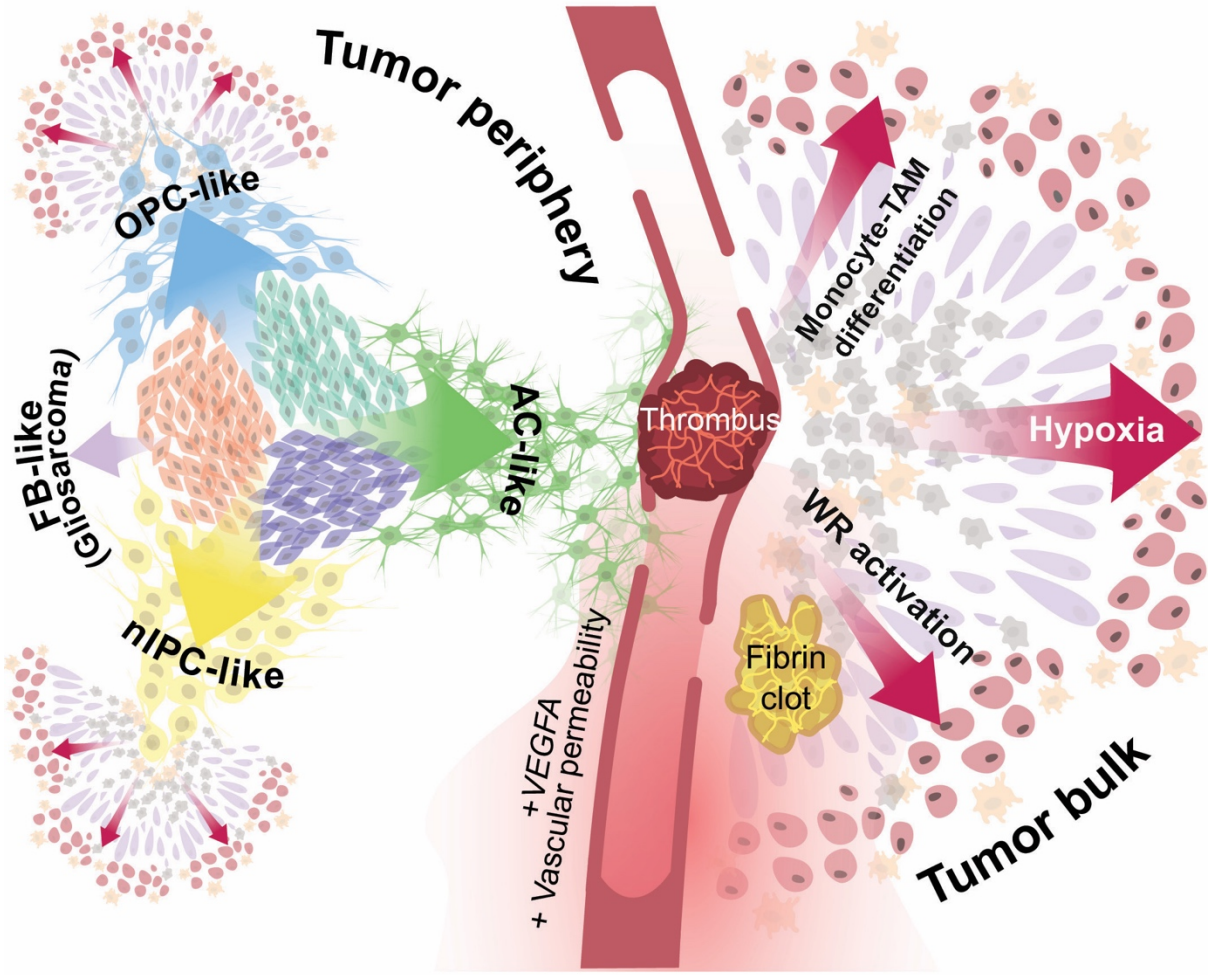

Extended Data Figure 10. Model of GBM organization by wound response. Glia-like cell states proliferate and drive tumor growth. Tumor bulk formation brings about tissue disruption, vascular dysfunction, hypoxia, promoting hemostatic responses and monocyte infiltration. Consequently, WR states are activated, monocytes are sequestered and differentiate into TAMs, perpetuating the futile wound response.

1169 **SUPPLEMENTARY INFORMATION**

1170 **Supplementary Table 1. Reanalysis of mesenchymal cell states in glioblastoma.** Excel workbook
1171 containing the results of gene ontology analyses of mesenchymal-like cell states from Phillips *et al*.[8],
1172 Verhaak *et al.*[1] and Neftel *et al.*[5] Each tab contains the results from one such analysis and includes
1173 links to the original publication, the gene set used, and a list of all statistically significant gene ontology
1174 terms with statistics.

1175 **Supplementary Table 2. Wound response signature gene list.** Ranking of all genes in the bulk vs
1176 periphery from scRNA-seq data. The average ranking for genes in three major cell types (tumor cells,
1177 macrophages + TAMs, oligodendrocytes) and across both multi-region samples (SL040 and SL057).
1178 The top 500 ranking genes are displayed, with the highest-ranking gene on the top.

1179 **Supplementary Table 3. Clinical data and pathology report summary.** Includes pseudonymized
1180 patient data and corresponding samples used for scRNA-seq, EEL-FISH and organoid experiments.

1181 **Supplementary Table 4. Primer and probe panels.** EEL-FISH encoding and readout probes, primers
1182 and the Xenium gene panel are listed in separate tabs. The Atto 590 EEL-FISH panel was only used
1183 for back-up detection of genes included in other panels.